ΠΑΝΕΠΙΣΤΗΜΙΟ ΚΡΗΤΗΣ
ΣΧΟΛΗ ΘΕΤΙΚΩΝ ΕΠΙΣΤΗΜΩΝ

ΤΜΗΜΑ ΦΥΣΙΚΗΣ

Χρονικός Χαρακτηρισμός παλμού Τρίτης Αρμονικής (267nm) μικρής χρονοδιάρκειας

Μεταπτυχιακή εργασία

Παπαλαζάρου Ευάγγελος

Υπεύθυνος Καθηγητής: Δ. Χαραλαμπίδης

ΗΡΑΚΛΕΙΟ 2005

UNIVERSITY OF CRETE
SCHOOL OF SCIENCES

DEPARTMENT OF PHYSICS

Temporal Characterization of an ultra-short Third Harmonic (267nm) pulse

Master Thesis

Papalazarou Evaggelos

Thesis Supervisor: D. Charalambidis

HERAKLION 2005

Ευχαριστίες

Η εργασία αυτή είναι αποτέλεσμα της συνεργασίας μιας ομαδας ανθρώπων τους οποίους θα ήθελα να ευχαριστήσω.

Αρχικά, θα ήθελα να ευχαριστήσω ιδιαίτερα τον κ. Δημήτρη Χαραλαμπίδη, Καθηγητή του Τμήματος Φυσικής της σχολής Θετικών Επιστημών του Πανεπιστημίου Κρήτης, για την πολύτιμη συνεργασία μας κατά τη διάρκεια εκπόνησης της εργασίας αυτής καθώς και για την γενικότερη εποπτεία της. Χάρις σε αυτόν μου δόθηκε η ευκαιρία να ασχοληθώ με τον τομέα της Ατομικής Φυσικής πολύ ισχυρών πεδίων ενώ παράλληλα μου άνοιξε τους επιστημονικούς μου ορίζοντες και με έκανε να δω την εργασία αυτή σαν μία πρόκληση.

Θα ήθελα στη συνέχεια να ευχαριστήσω τον κ. Κωνσταντίνο Φωτάκη, Καθηγητή του Τμήματος Φυσικής της σχολής Θετικών Επιστημών του Πανεπιστημίου Κρήτης και διευθυντή του Ι.Η.Δ.Λ του Ι.Τ.Ε., ο οποίος μου έδωσε την ευκαιρία να εργαστώ ερευνητικά στα εργαστήρια λέιζερ κατά τη διάρκεια διακπεραίωσης των πειραμάτων.

Ένα ιδιαίτερα μεγάλο ευχαριστώ θα ήθελα να εκφράσω στους Δρ. Πάρη Τζάλλα, Ερευνητή Δ' του Ι.Η.Δ.Λ, και Δρ. Milutin Kovacev, για την ενθαρρυντική τους στάση, την πραγματικά πολύτιμη βοήθειά τους καθώς και για το ενδιαφέρον που έδειξαν για τη διεξαγωγή των πειραμάτων. Οι ιδιαίτερα χρήσιμες συζυτήσεις μαζί τους αλλά και οι επιστημονικές τους γνώσεις υπήρξαν καθοριστικές για την αποπεράτωση της εργασίας αυτής.

'Ενα ευχαριστώ οφείλω και στον Δρ. Jonathan Plumridge, για την πολύτιμη βοήθεια και καθοδήγησή του για μια μεγάλη χρονική διάρκεια από την αρχή της εργασίας αυτής. Σε αυτόν οφείλεται και ένα μεγάλο μέρος του κώδικα της διάδοσης της οπτικών ακτίνων μέσω γεωμετρικής οπτικής (ray-tracing) της πειραματικής διάταξης.

Είμαι πραγματικά ευγνώμων στον κ. Γιάννη Λαμπράκη και ιδιαίτερα στη κα. Αντωνία Μπονάρου για την, επί καθημερινής βάσεως, συντήρηση αλλά και επίλυση των προβλημάτων του λέιζερ.

Ακόμα, θα ήθελα να ευχαριστήσω: τον κ. Γιώργο Παπαϊωάννου, ο οποίος σε συνεργασία με τον Δρ. Milutin Kovacev, κατέστησε ικανή την αυτόματη απόκτηση δεδομένων κάνοντας έτσι εφικτή την εύκολη διεξαγωγή των πειραμάτων, τον κ. Αποστόλη Εγγλέζη, για την παροχή πολλών λειτουργικών μερών της πειραματικής διάταξης, και τον Δρ. Μανώλη Μπενή για τις πολύτιμες συμβουλές του για θέματα πειραματικού κενού.

Δε θα πρέπει να παραλείψω να εκφράσω τις ευχαριστίες μου και στους μεταπτυχιακούς φοιτητές του εργαστηρίου των λέιζερ. Η φιλική παρουσία τους στο χώρο των εργαστηρίων κάνει την εργασία ευχάριστη και επικοδομητική. Τέλος, ένα μεγάλο

ευχαριστώ οφείλω στην οικογένεια και στους φίλους μου για την υποστήριξή τους που με τον έναν ή τον άλλον τρόπο, ήταν για μένα πολύτιμη.

Βαγγέλης Παπαλαζάρου,

Μάρτιος 2005

Contents

Abstract

Nowadays, it is well established that the superposition of higher-order harmonics (HOH), as a result of the non-linear response of matter to intense laser pulses (greater than 10^{13} W/cm^2), comprises an avenue towards ultra-short pulses in the attosecond time-scale. Although this approach has significant advantages there are still a number of difficulties one has to surmount. A blind superposition of harmonics will result on loss of all short-time-structure of the field. Thus, it is of great importance to know their temporal characteristics.

In this framework an experimental method has been proposed for the measurement of the relative phase distribution of the spectral components of a superposition of higher-order harmonics or the phase distribution of individual ones. This method is based on the "phase-control" of the excitation probability between the harmonic radiation and its fundamental source. The work of this Thesis is focused in implementing, for the first time, this proposed method to directly measure the phase distribution of a short third harmonic pulse generated by a Ti:Sapphire laser system. In implementing this we used a proposed experimental set-up based on a transmission grating interferometer having the advantage to be dispersionless. From the retrieved phase and the measured spectral amplitude distribution the temporal profile of the measured third harmonic pulse could be reconstructed. This work opens-up a new route to characterize harmonics, which can be extended to the temporal characterization of XUV pulses of ultra-short pulse duration.

Chapter 1

Introduction

1.1 Breaking the femtosecond barrier

During the last decades, the evolution of the lasers to the femtosecond (1-fs = 10^{-15} s) time-scale by simultaneously achieving unprecedented high intensities triggered a variety of new applications and achievements in the fields of atomic, molecular and solid-state physics. Some years ago, it was known that light-atom interactions are depended strongly on the duration of the light pulses [1]. The use of short femtosecond laser pulses that contain only a few oscillations of the electromagnetic field gave us the possibility to create a narrow time-window through which many atomic and molecular phenomena could be explored. But, our quest to explore deeper such phenomena, where even finer time resolution is required, fuels the drive towards shorter pulses. Given that an optical pulse could not be shorter than one cycle of the electromagnetic field and that the current used femtosecond lasers (e.g. Ti:Sapphire) have wavelengths in the visible or near-infrared spectral regime, it was believed that the down threshold of the pulse duration was reached to about few fs [2].

Breaking the femtosecond (1-fs) barrier, thus entering into the attosecond (1-as = 10^{-18} s) time-scale regime, was a challenging target for many years. The breakthrough came just in the last decade by providing several proposals [3,4,5] for the generation of attosecond pulses based on the Fourier-synthesis of an appropriately phased comb of equidistant frequencies and thus mimicking the technique of mode-locking in femtosecond lasers. This technique shortly led to what is known these days as High-

order Harmonic Generation (HOHG) [6]. The superposition of these harmonics has been proposed as a candidate towards to generation of ultra-short pulses of sub-femtosecond duration, which, when thoroughly available and characterized, will be the fastest camera ever created.

1.2 Towards to attosecond pulse metrology

Despite the advantages of this technique for the generation of attosecond light pulses, there are still many problems that one has to surmount. Among them, the blind superposition of a large number of harmonics with wrong spectral relative phase distribution may easily destroy all the attosecond time-structure of the field. Thus, it is vital to know their temporal characteristics – relative phase distribution and amplitudes – in order to be superimposed in a controllable way. This problem possesses a forefront in the attosecond science.

To characterize attosecond pulses is quite a challenge. Besides their extremely short duration they have spectral components lying in the XUV spectral regime with rather low intensities. The latter comprised the major obstacle in using the standard short pulse metrology such as second or higher order autocorrelation techniques by using non-linear crystals as well as because of their photon energies made impossible the use of beam-splitters. The last few years many efforts have been directed towards new methods of pulse metrology. Some of them are based on cross-correlations between the harmonics and their source infrared (IR) field. These methods are able to provide information on the relative phase distribution between the harmonics, but they do not account for the frequency modulation (chirp) inside their bandwidth. The presence of the chirp could play a crucial role to their superposition and thus it should be taken into account.

An alternative way has been proposed in order to fully map out the phase distribution of the superimposed harmonics thus providing information also on the chirp within their bandwidth. This method is based on what is known as phase-control of excitation processes. Furthermore, a suggested experimental arrangement has provided the appropriate tool for the implementation of this method by utilizing a freestanding

transmission grating in order to overcome the problems of the absorption introduced by the beam-splitters.

1.3 The Scope of this Thesis

The motivation in this Thesis is the implementation, for the first time, of the above proposed method of using the transmission grating interferometer to phase-control the excitation processes probed by individual harmonics or superimposed ones and the correlated IR laser pulse. In particular, the present work is focused on the temporal characterization of the third harmonic pulse generated from a Ti:Sapphire laser, thus giving the first experimental results for a step towards to the characterization of higher order harmonics.

The reader will find this Thesis organized as follows. Chapter 2 introduces the reader to the harmonic generation processes as a result of the non-linear response of matter to intense strong laser fields. Furthermore, a brief overview of the different ionization regimes is presented, in which harmonic generation is described by different mechanisms.

Chapter 3 presents a detailed review of the currently available techniques used to provide the necessary information for the characterization of ultra-short pulses. This Chapter is, finally, focused on the extension of some of these techniques to the attosecond time-scale, presenting the current difficulties and progress in characterizing high order harmonics.

Chapter 4 examines the cross-correlation technique based on the phase-control of the excitation processes. A detailed description of this method is provided and is based on formulated general predictions and simulations towards the characterization of high order harmonics. The work is, finally, focused on the implementation of this technique to the characterization of the TH pulse by providing a quantitative example for the influence of the chirped TH pulses to the cross-correlation interferograms.

Chapter 5 includes a detailed description of the experimental set-up used and the difficulties encountered in implementing the present work. Furthermore, we present a ray-tracing analysis adapted to the used experimental set-up in order to provide its dispersionless characteristics. Finally, we present the first experimental results on utilizing this method as well as aspects for future experiments.

Chapter 2

Interaction of atoms with strong laser fields

2.1 Introduction

Harmonic generation is the result of the non-linear response of matter to intense laser radiation. This non-linear response manifests itself in a non-linear dependence of the induced time-varying dipole moment on the electric field of the incident radiation. The non-linearity has an explicit dependence on the intensity. Thus, at low and moderate intensities, where the laser field can be treated as weak, the induced dipole moment oscillation, following the laser field, is dominated by the laser frequency. On the other hand, at high intensities, where the laser field is strong, frequency components of the dipole moment appear at multiples of the laser frequency (i.e. harmonics) acting as a radiation source.

In following it is introduced how this non-linear behavior of matter leads to harmonic generation. In particular, Section 2.2 deals with the interaction between an atom and an incident short laser pulse, in which depending on its intensity and wavelength, many interesting phenomena can be observed, such as multi-photon absorption, multi-photon ionization and above-threshold ionization. The different mechanisms used in order to describe these phenomena are shortly presented. These phenomena are synonyms to the different laser-atom interaction regimes within which harmonic generation is described by the appropriate model. Section 2.3 briefly describes the harmonic generation in these different interaction regimes.

2.2 Interaction of an atom with a strong laser field

In this Section we describe the interaction processes that take place between the strong electric field of an intense short-laser-pulse and an atom. Here, the meaning of intense is as follows. The laser field has to be compared with the static Coulomb electric field that an electron experiences in an atom. The magnitude of the electric field in the ground state of a hydrogen atom is equal to ~ 5×10^9 V/cm (i.e. $E_C \sim -k\,e\,/\,a_B^2$, where a_B is the Bohr's atomic radius, e is the electron charge and k is the Coulomb constant). A laser field is strong when approaches the field experienced by a valence electron in the Coulomb potential. Thus, the atomic unit of the electric-field-strength has to be of this order of magnitude. Therefore, the intensity of the laser needed to reach these field-strengths is of the order of 3×10^{16} W/cm^2. Such incident laser intensities completely distort the Coulomb binding potential of the atom. The atom cannot survive under these conditions for a long-time and consequently, it undergoes field-ionization. The ionization is a process that occurs in almost every interaction of a strong laser field with atoms and is of crucial importance to understand its mechanisms. Depending on the laser intensity and wavelength, the mechanisms vary and the models used in describing them are well established. Below, we present a brief overview of some of these mechanisms and related literature.

When the electric field of the laser is much weaker than the static Coulomb field, it does not alter the Coulomb potential. The atom-field interactions can be manipulated using the lowest-order perturbation theory (LOPT) [1,2]. However, the electric field, even under these circumstances, can be strong enough to induce non-linear processes. Therefore, the atom is ionized by absorbing n low-energy photons, with n being the minimum number of photons needed to exceed the ionization potential. This process, called multi-photon ionization, is depicted in Figure 1.1(a), where V_C is the Coulomb potential and r the distance of the electron from the nucleus. The n-photon ionization rate is proportional to I_0^n, where I_0 is the intensity of the laser (see Appendix A). Depending on the wavelength of the laser, this intensity dependence can also break down when the laser intensity reaches a critical value, I_S, above which ionization saturates [3]. By saturation is meant that population depletion occurs, where almost all the atoms have been ionized. As the intensity of the incident light increases, the atomic

energy levels start to shift in a dynamic fashion, a phenomenon called AC-Stark shift [1,2]. In this case, the energy-shift for weak bound states (Rydberg states) and for the ionization threshold is equal to the time-average kinetic energy of a free electron that it gains as it oscillates in the field. This quiver energy is called ponderomotive energy and is given by

$$U_p = \frac{e^2 E_0^2}{4m\omega_0^2}, \tag{2.1}$$

where e is the electron charge, E_0 is the instantaneous electric field, m is the electron mass and ω_0 is the angular frequency of the laser field. Although this process is non-perturbative, high order perturbation theory can be used for an estimation of the n-photon ionization rate.

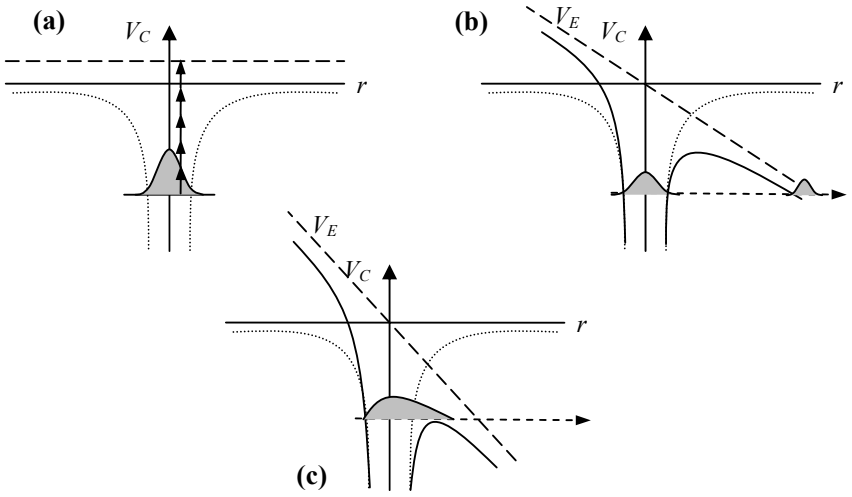

Figure 1.1: A schematic diagram that shows the three ionization regimes. (a) The multi-photon regime. The dotted curves depict the Coulomb binding potential V_C and the dashed line depicts the continuum state, where an electron is excited by e.g. five-photon absorption. (b) The tunneling regime. The dashed line depicts the external laser electric field V_E. (c) The over-the-barrier ionization regime, where the electron (is represented as a wave-packet) is free to escape.

If the oscillating laser electric-field-strength becomes comparable to the binding atomic Coulomb field, then an outer-shell electron can tunnel through the potential barrier with a substantial probability from its bound state before the laser electric field reverses its sign. This phenomenon is known as tunneling ionization. Figure 1.1(b) depicts this mechanism. The external electric field potential V_E is considered being proportional to $erE_0\cos(\omega_0 t)$, where E_0 is the electric field amplitude and ω_0 is the angular frequency of the oscillating laser field.

As the intensity of the laser becomes even higher, the binding potential barrier is suppressed further such that the initially bound electron is free to escape from the attraction of the atomic Coulomb potential. This process is called over-the-barrier ionization (Figure 1.1(c)). Typically, this ionization process dominates for laser intensities above 10^{15} W/cm^2 in rare gases. For even higher intensities, above 10^{18} W/cm^2, the electrons are accelerated to relativistic speeds by the laser field. At such high intensities very exciting phenomena can occur, such as plasma wake-field formation [4] or relativistic self-focusing and channeling [5]. A review of these ionization mechanisms is given in Ref. [6].

Keldysh in 1965 [7,8] introduced a governing quantity where the weak- and strong-field limits can be identified. This quantity is called Keldysh parameter, γ. The Keldysh parameter is an approximate indicator as to the applicability of the tunneling ansatz. It is essentially the time it takes the electron to travel through the potential width compared with the laser period T_0. Thus,

$$\gamma = \frac{T_{tunnel}}{T_0} = \sqrt{\frac{I_p}{2U_p}}, \tag{2.2}$$

where I_p is the ionization potential and U_p is the ponderomotive energy. By substitution of the eq. (2.1) to eq. (2.2) we see that $\gamma \propto \sqrt{2\omega_0^2 I_p / I_0}$ where I_0 is the intensity of incident laser light. If $\gamma << 1$ then the time for tunneling is short and the tunnel ionization dominates. For low-frequency laser fields (e.g. visible and near-infrared spectral ranges) incident into rare gases the tunneling ionization occurs at intensities, typically, between 10^{14} W/cm^2 and 10^{15} W/cm^2 [7]. $\gamma \approx 1$ corresponds to an intermediate condition between these interaction regimes. In the other limit where $\gamma >>$

1, the laser period is shorter than the tunneling time and thus the multi-photon ionization dominates. Multi-photon ionization typically occurs for intensities below 10^{14} W/cm^2.

Whereas these ionization regimes have attracted the attention of several groups around the world, they are beyond the scope of this thesis, which deals with intensities below 10^{13} W/cm^2. At these intensities, low-order harmonics are efficiently generated and the lowest-order perturbation theory (LOPT) is valid. Nevertheless, for the sake of completeness, it is worth to look into the harmonic generation at these different ionization regimes.

2.3 Harmonic Generation

Depending on the intensity and wavelength of the incident to an atom laser pulse, different models provide the mechanism of the generation of low- or higher-order harmonics. In this Section, a brief overview of the physics underlying harmonic generation (HG) at different laser-field-strengths is given.

In strong laser fields the high-order harmonic generation spectra have a characteristic generic shape (Figure 1.2). It consists of a sharp decrease in conversion efficiency with the harmonic order, followed by an extended plateau where the harmonic intensity remains practically constant and an abrupt cut-off where the intensity falls rapidly to zero. Depending on the laser-field-strength each of these spectral regimes is described by the appropriate model. In a weak laser field, low-order harmonic generation can be described in the multi-photon picture, where photons of low-energy are absorbed and the atom is excited to a virtual state below the ionization threshold. From there it decays to the ground state by simultaneous emission of one single-photon of high energy. This process is described approximately by the LOPT. HOHG is a result of multi-photon absorption above the ionization threshold and deexcitation of the electron from the continuum states to the ground (initial) state. The perturbation theory is still valid and predicts a rapid decrease of the harmonic intensity with the order. In a strong laser field, the emission of harmonics forms a plateau that is extended up to very high orders, where the harmonic intensity varies weakly with order and subsequently a cut-

off where the harmonic intensity is rapidly felt to zero. In this intensity regime and for low-frequency driving fields HOHG is well described by the three-step model (also known as "recollision model") [8,9] that gives a semi-classical argument of the observed phenomenon. According to this approach, the single atom cut-off scales as approximately $I_p + 3.2U_p$, where I_p is the ionization potential while U_p is the ponderomotive energy. This cut-off position is in good agreement with that found in experiments [10,11]. In addition, this model provides an approximate picture of the observed periodic spectrum where only odd harmonics are emitted (peaks) with a periodicity of twice the laser frequency. This is in agreement with the dipole selection rules and the inversion symmetry of the atomic potential allowing the emission of only odd harmonics. Despite the over-simplifications of this model, a quantum-mechanical version of the model, verified its validity [12].

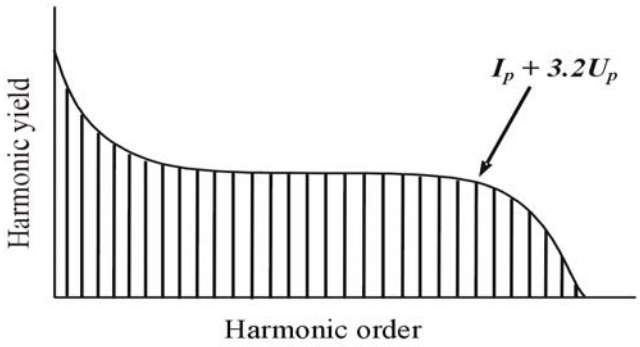

Figure 1.2: A schematic diagram of the generic shape of the high-harmonic spectrum.

The harmonic radiation has very interesting properties. Among them, the high-order harmonic radiation of the plateau regime appears to preserve the essential properties of a laser pulse. It possesses a good spatial and temporal coherence [13,14,15], it is highly directional [16,17] and it has a narrow bandwidth. Many applications relied on this fact. Among these applications, high-order harmonics made it possible to generate coherent extreme ultraviolet (XUV) and soft-X-ray radiation using commercial table-top lasers. Moreover, the coherent superposition of high-order harmonics offered the necessary bandwidth for producing even shorter pulses in the attosecond time scale.

Chapter 3

Ultra-short Pulse Metrology

3.1 Introduction

One of the greatest challenges in the femtosecond laser technology was to establish diagnostic techniques able to completely characterize these ultra-short pulses. The available metrology methods and the great progress on the material technology made this task shortly feasible. Although, this achievement reached an unprecedented resolution, the event of the generation of coherent sub-femtosecond pulses, turned many scientists to search for alternative methods. The fact that these pulses exist in the UV/VUV/XUV spectral regime made this task another challenge, since all the available materials used in femtosecond metrology are not transparent in these regimes.

This Chapter deals with these diagnostic techniques. Particularly, the next paragraphs summarize the available techniques and concepts used in femtosecond metrology. This discussion is further extended to the available methods and the existing difficulties in the metrology of pulses in the sub-femtosecond time-scale.

3.2 Diagnostic techniques in time domain

Because of the extremely short durations of the femtosecond laser pulses, there is no direct way to measure their temporal profile. The fastest electronic display instrument cannot resolve such time-scales. Thus, new techniques are designed to surmount these difficulties. These techniques are the subject of this Section.

3.2.1 The intensity cross-correlation

The temporal profile $I_S(t)$ of an optical pulse signal can be easily determined, if a shorter pulse, known as reference, of known shape $I_R(t)$ is available. The signal pulse then is measured by using the intensity cross-correlation, defined as:

$$S_C(\tau) = \int_{-\infty}^{+\infty} I_S(t) I_R(t-\tau) dt \,, \tag{3.1}$$

where τ is the delay between the pulses [1]. By this, the signal pulse $I_S(t)$ is varying in time with respect to the reference pulse. Every single part of the signal pulse is multiplied with every sigle part of the reference pulse and the product is integrated over the time.

The shape of the signal pulse can be determined by taking the Fourier-transform of the measured cross-correlation signal, $\widetilde{S}_C(\Omega)$, and dividing by the Fourier-transform of the known reference pulse, $\widetilde{I}_R(\Omega)$. The inverse Fourier-transform of the complex-conjugate of the ratio $\widetilde{S}_C(\Omega)/\widetilde{I}_R(\Omega)$ gives us the temporal profile of the signal pulse.

The correlation maximizes either when both pulses have the same shape and phase. Actually, this measurement reflects an indirect determination of their similarity as a function of the delay. Therefore, the measured signal is strong when they overlap and weak when the delay between them increases. In presence of noise, this operation leads to large errors unless the reference function is the shortest (temporally) of the two pulses being correlated. The ideal limit is when the reference is a delta-function. In this

case the shape of the signal pulse under investigation is identical to that of the correlated one. It is worth to point out here, the fact that the correlation function of the noise signal is a delta-function at $\tau = 0$. This provides an important feature in order to distinguish the signal from the noise. Unfortunately, even in this case, there is an important limitation in the information that can be retrieved from this method. It does not provide explicit phase information of the pulse being analyzed.

3.2.2 The autocorrelation technique

The fact that, a reference pulse much shorter than the signal pulse cannot always be generated, leads to the use of another technique where the signal pulse itself can be used as a reference. In this limit case the expression (3.1) has to be changed by the substitution $I_R(t) = I_S(t) = I(t)$, and the yielded function is called intensity auto-correlation. The Fourier-transform of the intensity autocorrelation is a real function, given as

$$\widetilde{S}_C(\Omega) = \left|\widetilde{I}(\Omega)\right|^2. \tag{3.2}$$

Thus, the intensity autocorrelation provides only very little information on the shape of the pulse. This particular autocorrelation technique will be discussed in detail in a followed sub-Section. Nevertheless, the autocorrelation is the most widely used diagnostic technique because of its property to be easily implemented.

3.2.2.1 The field autocorrelation

One of the most commonly used autocorrelation methods is the field autocorrelation, also known as first order autocorrelation. In this case, the optical pulse to be measured is split in two replicas and one pulse is variably delayed with respect to the other. The variation of the delay provides a characteristical interference pattern of the two optical fields $\int|E(t) + E(t - \tau)|^2 dt$. The recorded normalized signal is given as

$$g_1(\tau) = \frac{\int_{-\infty}^{+\infty} \left| E(t) + E(t-\tau) \right|^2 dt}{2\int_{-\infty}^{+\infty} \left| E(t) \right|^2 dt}, \tag{3.3}$$

where τ is the variable delay. The denominator indicates the background signal that corresponds to the signal in the wings of the interferometric trace, i.e. $g_1(\tau = \infty) = 1$. At the center of the trace, the signal maximizes, having a peak value of $g_1(\tau = 0) = 2$ and giving a standard peak to background ratio 2 to 1. Decomposition of the eq. (3.3) gives a background-free signal proportional to $\int E(t)E(t - \tau)dt$. The Fourier-transform of the latter expression is equivalent to the spectral intensity of the pulse and thus provides information only on the coherence length of the pulse and no information on its temporal profile and phase. For better knowledge of the pulse higher order auto-correlation is required.

3.2.2.2 Second order autocorrelation

The first attempt to measure an ultra-short pulse's intensity distribution in the time domain was based on this technique. It involves splitting a pulse in two replicas, variably delaying one pulse with respect to the other, and spatially overlapping them in some instantaneously responding nonlinear optical medium, such as a second harmonic generation (SHG) crystal (see Figure 3.1). A SHG crystal (e.g. a KDP or BBO) will produce radiation having twice the frequency of the input light and with intensity proportional to the product of the intensities of both pulses

$$I_{SHG} \propto I(t)I(t-\tau) \tag{3.4}$$

The measured signal reads

$$g_2(\tau) = \frac{\int_{-\infty}^{+\infty} I(t)I(t-\tau)dt}{\int_{-\infty}^{+\infty} I^2(t)dt}, \tag{3.5}$$

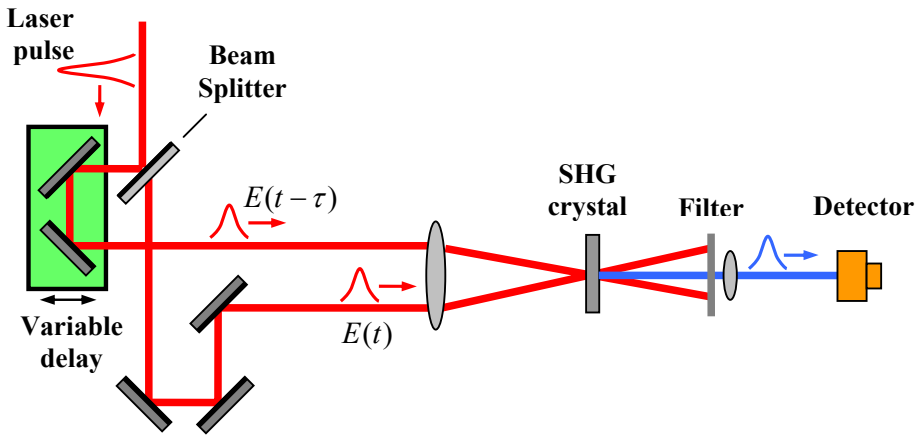

Figure 3.1: Experimental optical layout for a background free intensity autocorrelator using second harmonic generation. An input pulse is split into two replicas, one is variably delayed with respect to the other, and the two pulses are spatially overlapped in a SHG crystal (e.g. BBO). The second harmonic signal of the pulse sequence is detected, after passing through a color filter (to eliminate the fundamental beam), by the detector (e.g. photodiode or PMT).

which refers to a background-free second order autocorrelation signal. Figure 3.2 depicts two pulse shapes and their calculated intensity autocorrelation signals. One can notice that, although, a pulse duration can be retrieved to a satisfactory degree, by assuming a known pulse profile that fits to the data, the method is limited by the lack in providing explicit phase information. In fact, this shortcoming is most evident in complicated pulse shapes. Consequently, the pulse profile cannot be reconstructed by this method.

If the measurement is performed by recombining both pulses, after delaying one with respect to the other, in the SHG crystal (see Figure 3.3), then the second harmonic signal is proportional to

$$I_{SHG} \propto \int_{-\infty}^{+\infty} \left| (E(t) + E(t-\tau))^2 \right|^2 dt \,, \tag{3.6}$$

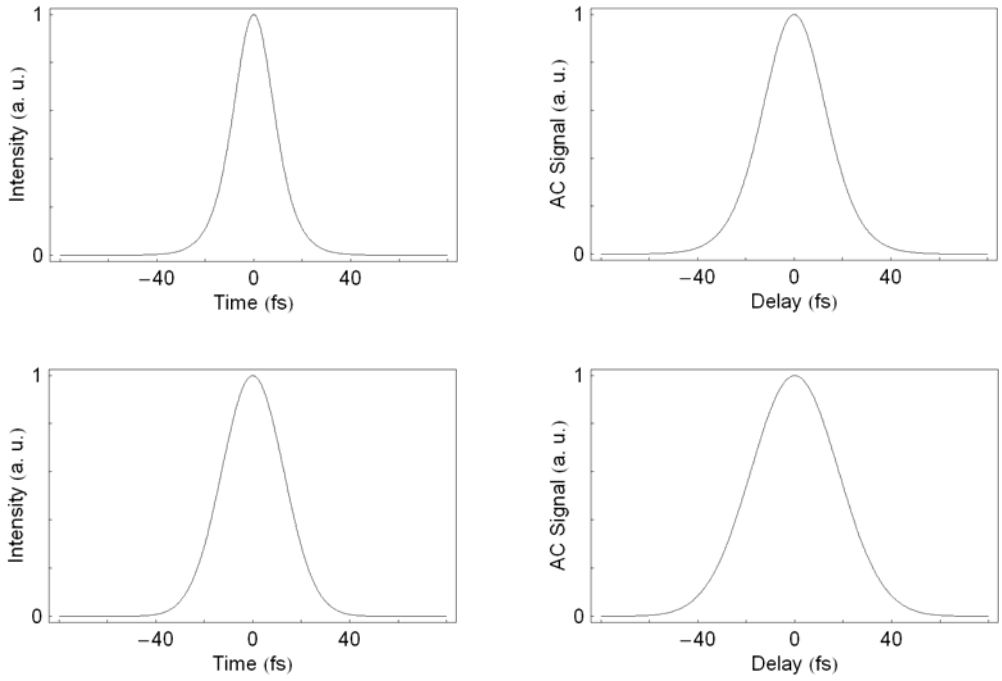

Figure 3.2: Simulated pulse shapes and background-free intensity autocorrelations, of a $sech^2$ pulse (top row) and a Gaussian pulse (bottom row).

which contains a constant background signal $I^2(t) + I^2(t - \tau)$, independent of the delay τ. The measured signal is known as second order interferometric autocorrelation, given by [2]

$$g_2(\tau) = \frac{\int_{-\infty}^{+\infty} \left| [E(t) + E(t-\tau)]^2 \right|^2 dt}{2\int_{-\infty}^{+\infty} \left| E^2(t) \right|^2 dt}. \tag{3.7}$$

By substitution of an electric field $E(t) = f(t)\exp[i\omega t + i\varphi(t)]$, to the eq. (3.7), leads to the following decomposition

$$g_2(\tau) \propto \int_{-\infty}^{+\infty} |f(t)|^4 dt + \int_{-\infty}^{+\infty} |f(t-\tau)|^4 dt + 4\int_{-\infty}^{+\infty} |f(t)|^2 |f(t-\tau)|^2 dt +$$

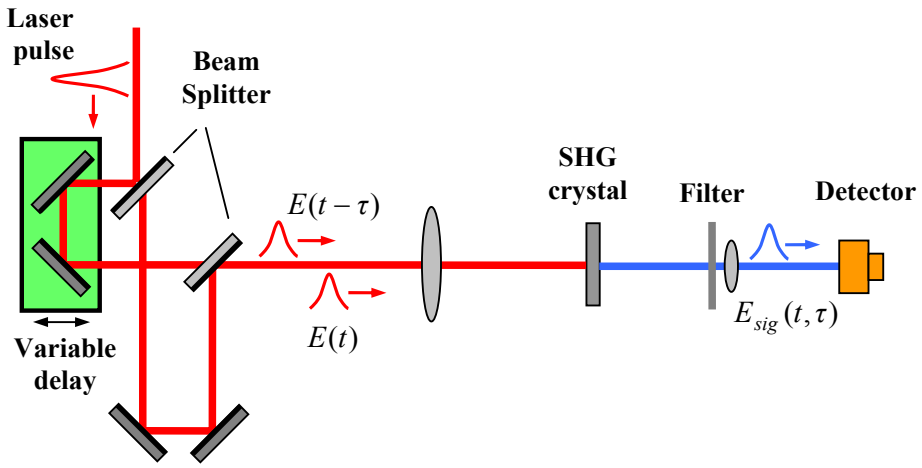

Figure 3.3: Experimental optical layout for an interferometric autocorrelator using second harmonic generation. An input pulse is split in two replicas, one is variably delayed with respect to the other, and the two pulses are recombined in a SHG crystal (e.g. BBO). The second harmonic signal of the pulse sequence is detected, after passing through a color filter (to eliminate the fundamental beam), by the detector (e.g. photodiode or PMT).

$$+2\int_{-\infty}^{+\infty}\left[|f(t)|^2+|f(t-\tau)|^2\right]f(t)f(t-\tau)\exp[i\omega\tau+i\varphi(t)-i\varphi(t-\tau)]dt+c.c$$

$$\int_{-\infty}^{+\infty}f^2(t)f^2(t-\tau)\exp[i2\omega\tau+i2(\varphi(t)-i\varphi(t-\tau))]dt+c.c\,. \qquad (3.8)$$

The purpose of the decomposition (3.8) is to show that the interferometric auto-correlation consists of three frequency components centered at zero frequency, ω and 2ω, respectively. The first two terms of the expression represent the background signal of each pulse separately at large delays ($\tau=\infty$). The third term is the intensity autocorrelation of the two pulses. The forth term looks like the interferogram of the electric field at frequency ω weighted by the sum of the intensities. The final term is the interferogram of the recorded second harmonic signal oscillating at 2ω. When all the terms of the interferometric signal are recorded then, at zero delay ($\tau=0$), add to give a coherent superposition of the fields of each pulse

$$g_2(0) = 16\int_{-\infty}^{+\infty} |f(t)|^4 \, dt \,. \tag{3.9}$$

The peak to background ratio of the interferometric autocorrelation, therefore, is 8:1. Figure 3.4 depicts simulated characteristic interferometric signals for the case of a bandwidth limited and a linearly chirped Gaussian pulse, from a Ti:Sapphire laser (λ = 800nm). The presence of the linear chirp results to a formation of a tail-edge in the interferogram (shown as a blue curve). The FWHM of the curve that follows the tail indicates the duration of the pulse due to chirp, and the FWHM of the interferogram indicates the coherence time.

The expression (3.8) sometimes is getting difficult to be measured for complicated pulse-shapes. Thus, it is proper to use the mean-value of each optical cycle of the interferogram, which can be easily measured by using a slow-resolved detector or by scanning faster delays between the pulses. Therefore, the result signal is

$$A_C(\tau) = \int_{-\infty}^{+\infty} |f(t)|^4 \, dt + \int_{-\infty}^{+\infty} |f(t-\tau)|^4 \, dt + 4\int_{-\infty}^{+\infty} |f(t)|^2 |f(t-\tau)|^2 \, dt \,, \tag{3.10}$$

which is the DC term of the eq. (3.8), and it is known as “intensity autocorrelation with background”. This method can be exploited to provide only information about the duration of simple pulses, since it measures only the intensity of the pulse. The peak to background ratio, in this case, is 3:1.

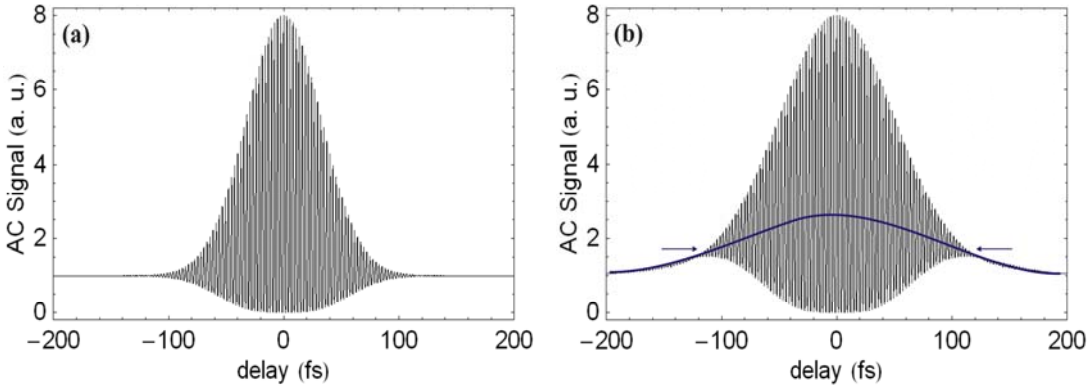

Figure 3.4: Numerical simulations of interferometric autocorrelations of a Gaussian pulse. (a) A 50-fs bandwidth limited pulse. (b) A 50-fs pulse with 2000 fs^2 of linear chirp.

3.2.2.3 Higher-order autocorrelation

The higher-order autocorrelation require a higher order non-linearity. Thus, the *n*-th order autocorrelation function is given as:

$$g_n(\tau) = \frac{\int_{-\infty}^{+\infty} \left| [E(t) + E(t-\tau)]^n \right|^2 dt}{\int_{-\infty}^{+\infty} \left| [E^n(t) \right|^2 dt}. \tag{3.11}$$

High order correlations are very convenient and powerful tools for the determination of intensity profiles. The higher the order of the autocorrelation function, the better the knowledge of the measured pulse.

3.3 Phase and amplitude retrieval techniques in time and frequency domain

In the previous Section we saw techniques using correlation methods in time domain in order to measure the duration of ultra-short pulses. For the full pulse reconstruction techniques able to retrieve the complete phase information is required. For years, the search of such a technique was a challenge, since the methods based on intensity autocorrelation [3-5] or later developments based on indirect determination of various phase distortions [2,6,7] were able to yield only partial information. Still other methods had been developed to yield only the intensity $I(t)$ [8,9] or they required a streak camera [10,11] and hence lack sufficient temporal resolution. Some others were able to yield the phase $\varphi(t)$, but they were too complex and they didn't yield the intensity distribution [12-14].

A remarkable progress had occurred in the development of techniques in the time and frequency domain. These are techniques well known from acoustics and can fully characterize a temporal event. Many attempts had been carried out to characterize optical pulses by using these ideas. An important one came in light in the early 90s' by J. Chilla and O. Martinez [15-17], which had demonstrated a method able to directly

provide the pulse-shape and frequency in the frequency domain by using sonograms [18]. Others have since developed variations of this method [19,20]. Unfortunately, the technique was too complex and unable to perform single-shot operations making it a difficult to use technique.

The breakthrough in the full characterization of ultra-short optical pulses occurred ten years ago by Rick Trebino and Daniel Kane with the introduction of the Frequency Resolved Optical Gating (FROG) [21-23]. The method is an accurate and rigorous technique that can be employed for the characterization of arbitrary pulses [24,25]. In addition, non *a priori* information about the pulse-shape is necessary to reconstruct the pulse from a FROG trace, something common to any conventional autocorrelation based measurements.

3.3.1 Frequency resolved optical gating (FROG) and its geometries

The FROG is an autocorrelation-type method, which resolves a pulse signal as a function of the delay and frequency, using a two-dimensional spectrogram [26]. The resulting spectrogram, known as FROG trace (see Figure 3.5a), can be analyzed to retrieve the full pulse intensity distribution and the phase using an iterative algorithm. In general, the measured FROG trace is given

$$S_g(\tau,\Omega) = \left| \int_{-\infty}^{+\infty} E(t) g(t-\tau) \exp(-i\Omega\tau) dt \right|^2 , \qquad (3.12)$$

where $g(t-\tau)$ is a variably-delay gate-pulse usually somewhat shorter than the signal to be analyzed but not infinitely short [23], otherwise the spectral phase information will be lost.

Figure 3.5(b) depicts a FROG configuration that comprises of splitting the pulse to be measured in two replicas, variably delay one pulse with respect to the other, and crossing them in an instantaneously responding non-linear medium, which is usually a Kerr optical-gate [21]. In this case the gate pulse equals to $|E(t - \tau)|^2$.

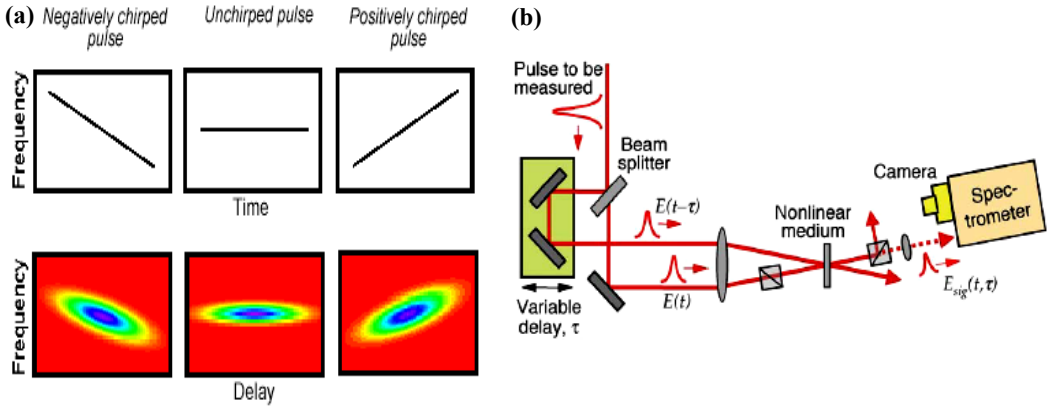

Figure 3.5: (a) Spectrograms (bottom row) for negatively chirped, unchirped and positively chirped Gaussian pulses reflect the pulse frequency vs. time respectively. (b) Experimental arrangement of FROG using a Kerr optical gate (polarization gate geometry).

Generally, FROG is a quite accurate autocorrelation method having many advantages over other techniques of this kind. A given pulse shape has always its own FROG trace. Thus two different pulse shapes result different FROG traces. In addition, the two dimensional trace and the huge number of the data points makes it less sensitive to noise. Another important aspect is the fact that it can be used for single-shot measurements [22,27].

Because there are several beam geometries, there exist several FROG variations, which can be used to perform FROG measurements. These variations are referred as polarization gate FROG (PG-FROG) [21,22,27,28], which is the simplest and mostly used method, the second harmonic generation (SHG-FROG) [21,23] and the third harmonic generation (THG-FROG) [29], which are second and third order auto-correlation techniques, respectively, the self-diffraction (SD-FROG) [23,30] and the transient grating (TG-FROG) [23,31]. Each of these yields its own traces, although, some geometries have similar traces [23]. Consequently, not every FROG geometry can be straightforwardly applied to measure ultra-short pulses of below 20-fs [32]. In particular, only the SHG-FROG and THG-FROG have been used as the best choice to measure pulses with duration below 10-fs, and this is due to their instantaneous non-linearity that misses from the other geometries. From these geometries the SHG based

FROG keeps the record of the shortest pulse measured from a Ti:Sapphire laser having a pulse-duration of 4.5-fs [33].

3.3.2 Spectral Phase Interferometry for Direct Electric-field Reconstruction (SPIDER)

An alternative technique of great importance came in light at late 90s' having the advantage to provide full characterization of the unknown optical pulse by using only a one-dimensional interferometric spectrogram without being necessary to use an iterative algorithm for the reconstruction of the spectral phase. This technique has been pioneered by C. Iaconis and I. A. Walmsley (1999) and is known as spectral phase interferometry for direct e-field reconstruction (SPIDER) [34,35]. It is based on the spectral-shearing interferometry of Froehly *et al*. [36], by which a replica of the unknown optical pulse is delayed with respect to the other and spectrally-sheared through sum-frequency generation [37] with two different frequencies provided by a third dispersed (chirped) pulse (Figure 3.6a). The resulting spectrum consists of fringes with a period $\sim c\tau$, where τ is the delay between the replicas and c is the speed of light in vacuum, by which the pulse can by completely characterized in time domain through a simple algebraic algorithm (i.e. finite number of steps) (Figure 3.6b).

Among the other techniques, mentioned above, the SPIDER has some noticeable advantages. First, it can eliminate the necessity for moving components making it easily implemented. Second, as an interferometric method, it requires the collection of less data than spectrographic ones and has a direct inversion algorithm that provides a very rapid pulse-shape reconstruction making it useful for real-time single-shot measurements [38]. Third, a thicker non-linear medium can be used by which, a higher intensity signal, as a result of a type-II phase matching for the sum-frequency generation between the ultra-broadband pulse and the quasi-CW field, can be achieved. Forth, and more important, it can be used for the characterization of few-cycle pulses of below 10-fs, and this is due to utilization of the sum-frequency light with the quasi-CW field [39,40]. Speaking of few-cycle pulses, a modified version of SPIDER can overcome the problem found of its low sensitivity due to drastic decrease in peak

intensity of strongly chirped reference pulses, by the use of a chirped seed pulse directly from the regenerative amplifier [41].

Generally, the SPIDER is found to be an essential technique for the characterization of a vast variety of pulses, having the advantage of measuring mono-cycle pulses with a measurement capability, which exceeds the one octave [40], in addition to the fast measurement time required.

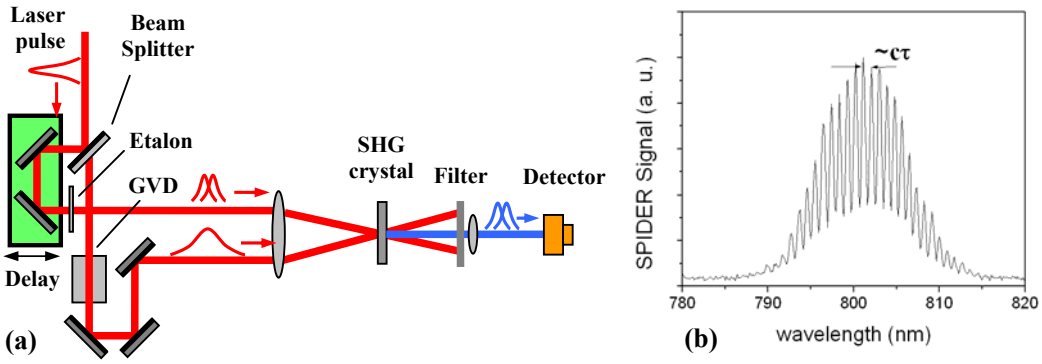

Figure 3.6: (a) SPIDER experimental arrangement, based on spectral-shear interferometry and (b) resulting interferogram consisting of fringes of period ~cτ (τ variable delay**).**

3.4 Diagnostic techniques extended in the sub-femtosecond time-scale

Although the generation of sub-femtosecond or attosecond pulses in laboratories, nowadays, is a fact, their temporal characterization still remains a quite difficult task. One of the major problems encountered was that their frequencies lie in the UV/VUV/XUV spectral range, where the crystals used as non-linear media in the autocorrelation methods to characterize femtosecond pulses, cannot be used. This problem has been overcome by using the two-photon ionization of rare gases. In particular, for sufficiently intense attosecond pulses, this method can be used as a non-linear process by which a correlation signal can be obtained. Generally, the characterization of weak UV/VUV/XUV pulses relies on the two-color atomic

ionization as the only usable non-linear process. Cross-correlation methods are based on this approach. In following we review the used diagnostic techniques and their latest progress in the attosecond pulse metrology.

3.4.1 The first experimental attosecond pulse indication

The first implemented autocorrelation technique used to confirm the existence of attosecond pulse trains from the superposition of high-order harmonics has been performed by Papadogiannis *et al.* (1999) [42]. A sub-femtosecond beating with a period of ~1.3 fs (see figure 3.7), was clearly observed, indicating the generation of sub-femtosecond XUV pulses. The resulted power spectrum showed up a modulation of $\sim 2\pi/\omega_L$ reflected the fact that harmonics were apart twice the frequency of the fundamental ω_L. Unlike the results and according to Corkum [43], "the production and measurement are entwined" pointing out that the measurement was not completely transparent, and a controversy, on its interpretation came in light [44,45].

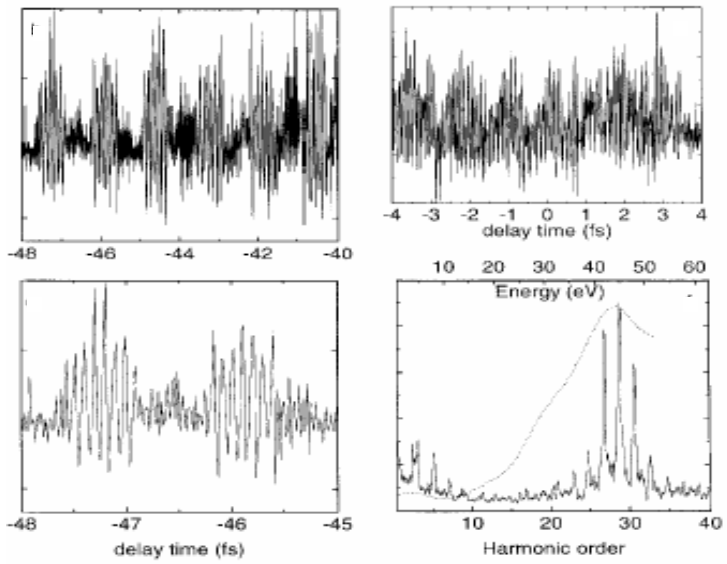

Figure 3.7: Total VIS-VUV-XUV signal filtered with a Al-Si filter as a function of delay of two harmonic generating laser pulses. (Top row) Expanded region of the leading edge and of the central part of the full signal. (Bottom row) Expanded region display one laser period and the power spectrum of the total trace (Papadogiannis *et al.* (1999)).

3.4.2 Intensity autocorrelation

A second-order autocorrelation method used in this spectral regime is based on the two-photon ionization of a rare gas by the XUV pulse used to be characterized. In particular, two replicas of the XUV pulse are initially delayed with respect to each other and then are focused in a rare gas whose ionization energy is such that two photons are required in order to eject one electron. The resulting signal is given by the second-order autocorrelation function.

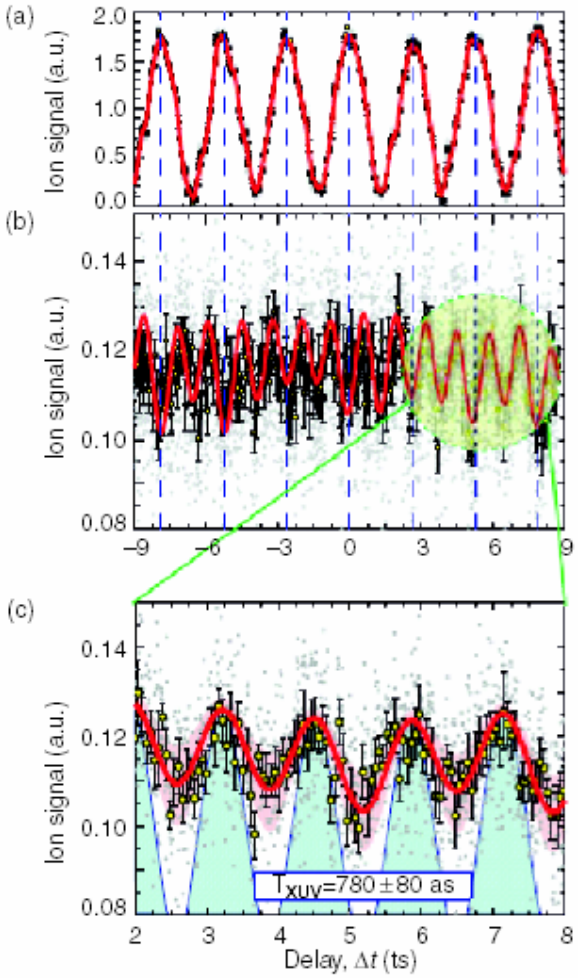

Figure 3.8: Intensity autocorrelation trace of an attosecond pulse train produced by harmonics 7-15 generated in xenon. This trace is the first direct measurement of a pulse train. The XUV bursts of the train have a duration of 780 ± 80 as. (P. Tzallas *et al*. (2003))

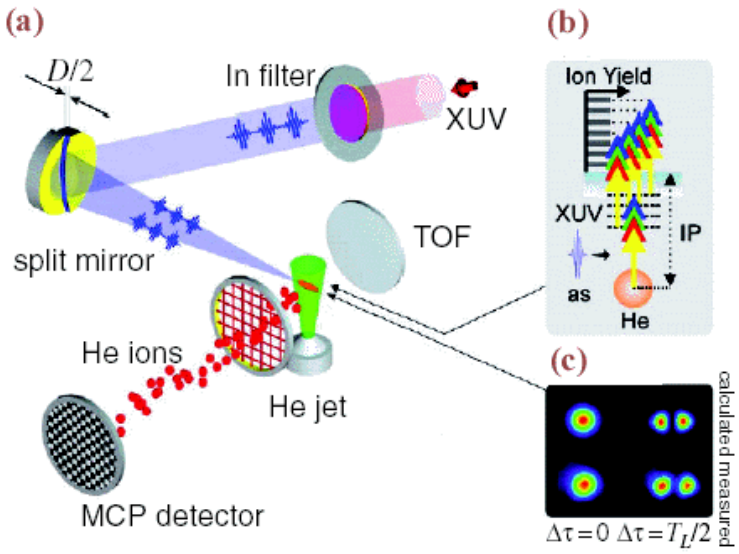

Figure 3.9: The second-order XUV autocorrelator. (a) A schematic representation of the experimental set-up used. (B) As a non-linear detector a two-photon ionized He gas is used. The ionization occurs through two-XUV-photon absorption from the all possible combination of the transmitted harmonics (7th -15th). (c) The zero and $\Delta\tau = T_L/2$ delay, the calculated and measured transverse intensity distribution of the for the IR laser pulse (P. Tzallas *et al*. (2003)).

Only few experiments had reported in the literature in the last few years, near resonant [46,47] and non-resonant [48-50] two-photon ionization, the 9th harmonic of of a Ti:Sapphire laser being used as the highest produced harmonic. Very recently, just two years ago, a demonstration based on this technique has been reported by P. Tzallas *et al*. who has recorded a second-order autocorrelation trace of a pulse train resulting from the coherent superposition of several harmonics - from the 7th to 15th [51], achieving of what was impossible till then. The non-linear signal detected was suitable for a second-order intensity autocorrelation showing an attosecond pulse train with pulses of duration 780 ± 80 as (see Figure 3.8). In achieving this, a wave-front splitting arrangement, consisting of a spherical mirror cut into two halves controlled by a piezo-crystal translation stage, was used. The two parts of the bisected XUV pulse train were focused into a He gas-jet that was two-photon ionized. The ions were detected as a function of the displacement between the two half mirrors (Figure 3.9).

3.4.3 Cross-Correlation: The two-color, two-photon ionization

An alternative method is to use the two-color, two-photon (or even multi-photon) ionization process by which the XUV is conversed with an intense infrared (IR) pulse†. In the presence of an IR field ω_L, the photoelectron energy spectrum from the photo-ionization of an atom by an XUV shows sidebands separated by ω_L. In the low-intensity limit these sidebands can be used as cross-correlation signal, since it is proportional to the convolution of the XUV and the IR pulses [52]. However, this method is hard to be used for attosecond pulses, since the IR pulse to be correlated with the XUV signal, is much longer.

3.4.4 FROG and SPIDER characterization of attosecond pulse trains.

FROG is indeed a very accurate and popular method in the metrology of femtosecond pulses, which can be extended to the attosecond regime by using a cross-correlation frequency-resolved optical gating (XFROG) [53]. Recently, Sekikawa *et al*. [54] and Norin *et al*. [55] have demonstrated, for the first time, the complete characterization of the fifth harmonic from a Ti:Sapphire laser using the XFROG. Since then, several groups [56], have worked intensively on this method, opening a route for the characterization of XUV pulses.

The extension of the SPIDER method to the XUV spectral range by Muller was not obvious [57] due to, at that time, existing problems with XUV beam-splitters and detectors. Very recently, J. Mauritsson *et al*. [58], proposed an alternative method in order to overcome these problems. According to them, two electron wave-packets are coherently produced by photo-ionizing atoms with two time-delayed replicas of the XUV. For one of the XUV pulses, photo-ionization occurs in the presence of a strong and long enough IR pulse that ponderomotively shifts the binding energy, thereby introducing a spectral shear needed for reconstruction of the spectral phase.

---

† In this case the ponderomotive energy is greater than the ionization potential and thus the process is non-perturbative.

3.4.5 The RABBITT method

The reconstruction of attosecond beating by interference of two-photon absorption (RABBITT) is an alternative method of measuring sub-femtosecond or attosecond pulses. Its principle is based on the three-color, two-photon ionization of a gas medium. According to Véniard *et al*. [59], the intensity of the IR is sufficiently low as for each harmonic to have only one sideband on either side of the initial XUV transition. Thus, the photoelectron energy spectrum consists of equidistant peaks. Peaks appearing at odd multiples laser photon-energies are caused by the superposition of odd harmonics and peaks appearing at even multiples laser photon-energies are caused by two-photon ionization, due to sum and different mixing of neighbor harmonics with the fundamental pulse (see Figure 3.10). As a consequence of the incoherence of the four excitation channels for each sideband, the modulation of the signal as a function of the delay of the IR field gives access to the relative phase between subsequent harmonics.

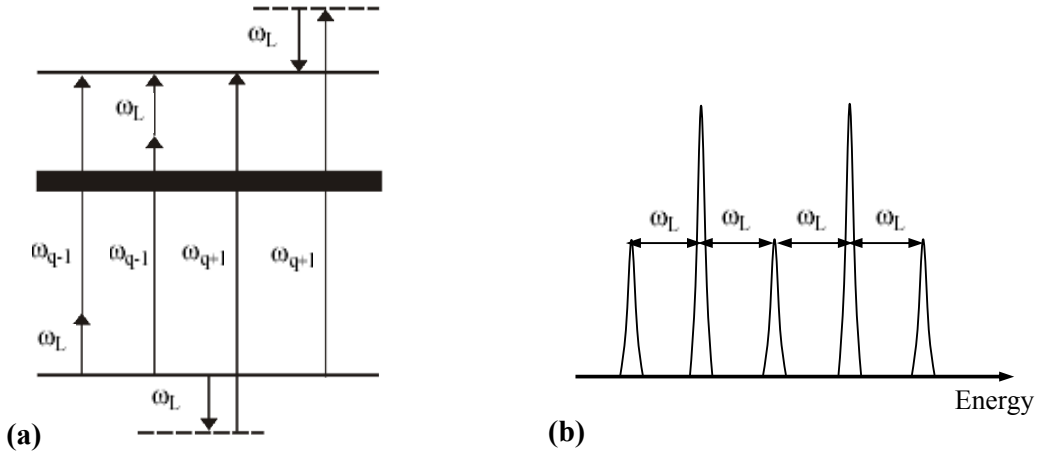

Figure 3.10: (a) The energy level diagram of the RABBITT method. The four excitation channels leading from the initial to the final level involve one and the subsequent harmonic and differ on the way that the photons are absorbed or emitted. (b) Photoelectron energy spectrum of the three-color ionization by two consecutive harmonics ω_{q-1} and ω_{q+1} and the fundamental ω_L. The middle sideband is shared by the two harmonics.

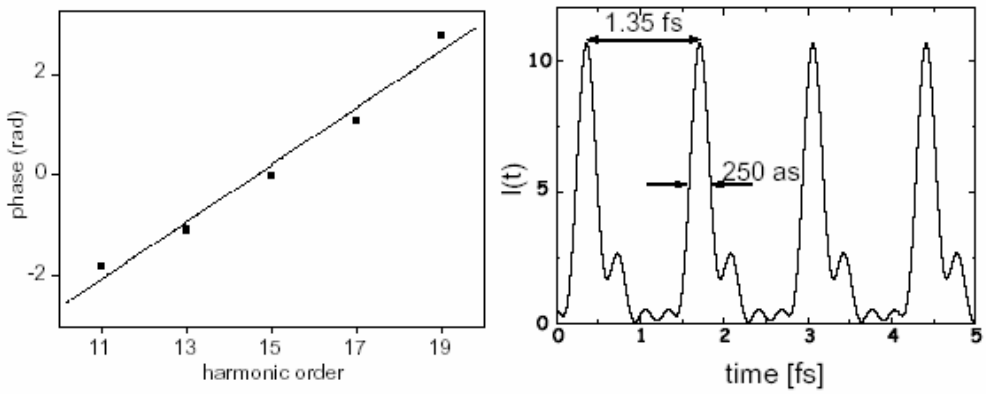

Figure 3.11: Relative phases (left) and temporal intensity profile (right) of a sum of five harmonics, reconstructed from measured phases and amplitudes. The FWHM of each peak is ~250 as. (P. H. Paul *et al.* (2001))

RABBITT has implemented by Paul *et al*. [60] who characterized harmonics from the argon plateau - from 11th to 19th (see Figure 3.11). On the other hand, there are some inherent limitations. For example, RABBITT does not account for the chirp within each harmonic and it tends to underestimate the pulse-duration due to spatio-temporal intensity effects [61, 62].

Chapter 4

A cross-correlation technique based on the "phase-control" of the excitation processes

4.1 Introduction

Among the presented methods mentioned in the preceding Chapter, the cross-correlation method provides a candidate solution, having the advantage of using a highly intense fundamental beam to characterize weak XUV pulses. These methods rely either on the dynamics of the ionization caused by harmonics in the presence of an IR field [1-3] or on phase-sensitive interference effects [4]. Although these methods provide information on the relative phase distribution between the harmonics, they do not account for the chirp within the bandwidth of each harmonic.

An alternative method that could fully map out the relative phase distribution between the superimposed or the phase distribution of individual harmonic modes has been proposed by E. Hertz *et al.* [5]. This method is based on the control of the excitation processes through the quantum interference of different coherent excitation paths that couple the same initial and final state of an atomic or a molecular system, with different number of photons [6-11]. Many demonstrations have been reported of how the process of phase-control can manipulate, the ionization of atoms, the dissociation of molecules and their dissociation branching ratios as well as the excitation in semiconductors, mainly in the nanosecond pulse duration regime. Moreover, control of harmonic generation based on this interference schemes for the high laser field

interactions, has been theoretically investigated by Charron *et al*. [12] and E. Cormier and P. Lambropoulos [13]. It is worth noting some experiments showing results of the coherent control of the ionization rate in four-photon resonant and five-photon ionization schemes of noble gases [14] or the control of near-resonant third harmonic generation through the phase of an additional third harmonic field [15]. In both of these experiments, a large interference modulation has been observed showing the advantage of this technique to control of harmonic generation.

This technique is the subject of this Chapter as it is underlying the experimental method employed in the present work. Particularly, in Section 4.2 we provide a detailed description of the "phase-control" of excitation processes. In Section 4.3 we address how this technique can be used for the complete characterization of attosecond pulses. Quantitative analysis is provided by numerical simulations on high-order harmonics of the perturbative regime. Finally, in Section 4.4, we apply this technique to the third harmonic (TH) field, as it is the harmonic of our interest.

4.2 The "phase-control" technique

Generally, this technique refers to the control of the excitation processes through the control of the relative phase between two different excitation paths that couple the same initial and final state of an atomic or molecular system. Two widely used descriptions of the processes are through the polarization of the atomic (or molecular) medium induced by the fundamental electric field, which is a macroscopic description of the processes and through the excitation probability of the atomic transitions, which refers to a microscopic point of view. In following a general description of this technique is provided. Furthermore, we describe of how this technique can be used to retrieve the spectral phase distribution of an incident radiation.

4.2.1 General concepts

Consider the atomic system of the Figure 4.1(a) and an experimental arrangement similar to that used for the coherent control of the third harmonic by D. Xenakis *et al*. [15] using nanosecond (ns) optical pulses. This experimental arrangement consists of a cell filled with an atomic gas medium for the generation of the TH, a "phase-shifting" cell used to delay each of the co-propagating beams, i.e. the fundamental and the TH, by varying the density of the atomic gas in the cell and thus introducing different optical paths due to the different refractive indices that the beams are seeing as they travel through it. Finally, both beams are focused into a third cell filled with an atomic gas medium. In the latter cell, TH is generated in the atomic medium through three different scattering processes (see Figure 4.1a), (a) three-photon absorption of the fundamental field ω and emission of one-TH-photon ω'_3, (b) one-TH-photon absorption ω_3 of that had generated in the first gas-cell and reemission and (c) one-photon absorption of the generated TH ω'_3 of and reemission of it. Therefore, the induced polarization $P_{3\omega}$ of the atomic system (medium) at 3ω consists of three interfering components, two linear and one non-linear

$$P_{3\omega} = \chi^{(3)}(\omega)E_1^3 + \chi^{(1)}(3\omega)E_3 + \chi^{(1)}(3\omega)E'_3, \qquad (4.1)$$

where $\chi^{(3)}(\omega)$ and $\chi^{(1)}(3\omega)$ is the third-order optical susceptibility at ω and first-order optical susceptibility at 3ω, respectively. $E_1(t)$ is the linearly polarized monochromatic fundamental field of frequency ω, $E_3(t)$ is its third harmonic (TH) field of frequency 3ω emitted in the second cell by one-photon absorption of the TH produced in first cell and $E'_3(t)$ is the TH field emitted in the second cell by one-photon absorption of the TH field produced in the second cell. The electric amplitudes and phases of the corresponding fields are E_{10}, E_{30} and E'_{30} and φ_1, φ_3 and φ'_3, respectively. Here the fundamental and harmonic fields are for simplicity assumed be monochromatic waves.

The first term of the eq. (4.1) represents harmonic generation while the second and the third term polarization at 3ω induced by the third harmonic of the corresponding electric field and the generated one in the medium. Equation (4.1) by substitution of the corresponding electric fields, can be written as

$$P_{3\omega} = \chi^{(3)}(\omega)E_{10}^3\,\mathrm{Re}\left[\exp(i3\omega t + i3\varphi_1)\right] + \chi^{(1)}(3\omega)E_{30}\,\mathrm{Re}\left[\exp(i3\omega t + i\varphi_3)\right] + \chi^{(1)}(3\omega)E'_{30}\,\mathrm{Re}\left[\exp(i3\omega t + i\varphi'_3)\right]. \quad (4.2)$$

The last equation can be simplified by assuming a constant relative phase between the fundamental and its generated third harmonic field $\varphi' = \varphi'_3 - 3\varphi_1 = \text{const.}$ during their propagation through the medium, which corresponds to the phase-matched condition.

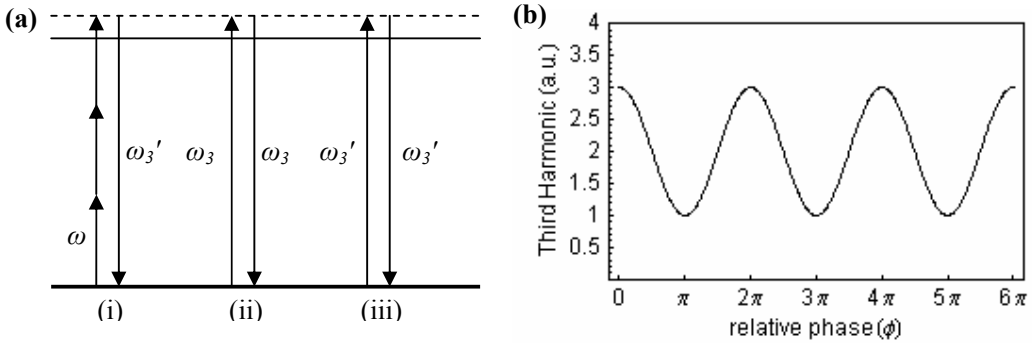

Figure 4.1: (a) Schematic representation of the three photon scattering processes, (i) through three-photon absorption of the fundamental and emission of one TH photon, (ii) through absorption of one-photon of the TH and re-emission and (iii) through absorption of one-photon of the generated TH and re-emission. (b) Constructive and destructive interference due to the relative variation of the phases between the induced polarization and the generated TH.

Then eq. (4.2) can be written as follows

$$P_{3\omega} = 2\,\mathrm{Re}\left\{\left[\left(\chi^{(3)}(\omega)E_{10}^3 + \chi^{(1)}(3\omega)E_{30}\exp(i\varphi')\right)\exp(i3\varphi_1) + \chi^{(1)}(3\omega)E_{30}\exp(i\varphi_3)\right]\exp(i3\omega t)\right\}. \quad (4.3)$$

or

$$P_{3\omega} = 2\,\mathrm{Re}\left[\left(\chi^{(3)}(\omega)E_{10}^3 + \chi^{(1)}(3\omega)E_{30}\exp(i\varphi')\right)\exp(i3\omega t)\right] + 2\,\mathrm{Re}\left(\chi^{(1)}(3\omega)E_{30}\exp(i\varphi)\exp(i3\omega t)\right) \quad (4.4)$$

as a function of the relative phase $\varphi = \varphi_3 - 3\varphi_1$ between the third harmonic of the total field and the fundamental one. The induced polarization, and thus the total TH field, oscillates as $\cos(\varphi_3 - 3\varphi_1)$ between maxima and minima. Consequently, constructive and destructive interference takes place due to variation of the relative phase φ (see Figure 4.1b)

The process can also be described through the excitation probability of the final atomic state coupled by the three quantum transitions of the Figure 4.2a that is given by

$$W \propto \left| \mu^{(3)} E_1^3(r,z,t) + \mu^{(1)} E_3(r,z,t) + \mu^{(1)} E_3'(r,z,t) \right|^2 , \tag{4.5}$$

where $\mu^{(3)}$ and $\mu^{(1)}$ are the third- and first-order electric dipole moment of the transition, respectively. In general, this way leads to the same results, since the linear and non-linear optical susceptibilities of the eq. (4.4) can be calculated numerically through the Schrödinger equation. Numerical predictions are particularly reliable for the case of atomic gases, because their internal atomic parameters – such as energy levels and dipole transition moments – that appear, generally, in the quantum mechanical expressions are often known with high accuracy. In addition, since the energy levels of the gas atoms are very sharp, it is possible to obtain significant large values for such parameters through the technique of resonance enhancement. This can be achieved, for example in the studied case of the third harmonic generation, when one of the photon-transitions is nearly resonant or on resonance with one real state of the atom [16].

4.2.2 Using the "phase-control" technique for the retrieval of the spectral phase distribution

Consider now an atomic system excited by an incident laser beam and by each harmonic. In the general case, the excitation occurs through different coherent pathways, and the most familiar scheme is by single-photon excitation through the *n*-th harmonic of the fundamental laser field and by *n*-photon excitation through the fundamental (see Figure 4.2). Both of these excitation paths couple the same initial $|0\rangle$

and final $|f\rangle$ state and consequently, quantum interference takes place. By varying the relative phase between the fundamental and the harmonic field, assuming both being monochromatic waves, the excitation probability of this particular state oscillates as a function of their relative phases, i.e. as $\cos(\varphi_n - n\varphi_1)$, where φ_n, φ_1 are the initial phases of the harmonic and the fundamental, respectively. This variation can be probed either through ionization – in the case where the final state is in the continuum [9,17] – or through harmonic generation – in the case where the final state is a virtual or a real state of the atomic system [12-15]. Probing with harmonic generation allows the study of interference below the ionization threshold and thus of lower harmonics as well. An important application of this method is that it can be used for the determination of the relative harmonic phase distribution and of the temporal profiles of a coherent superposition of harmonic fields or of individual harmonics.

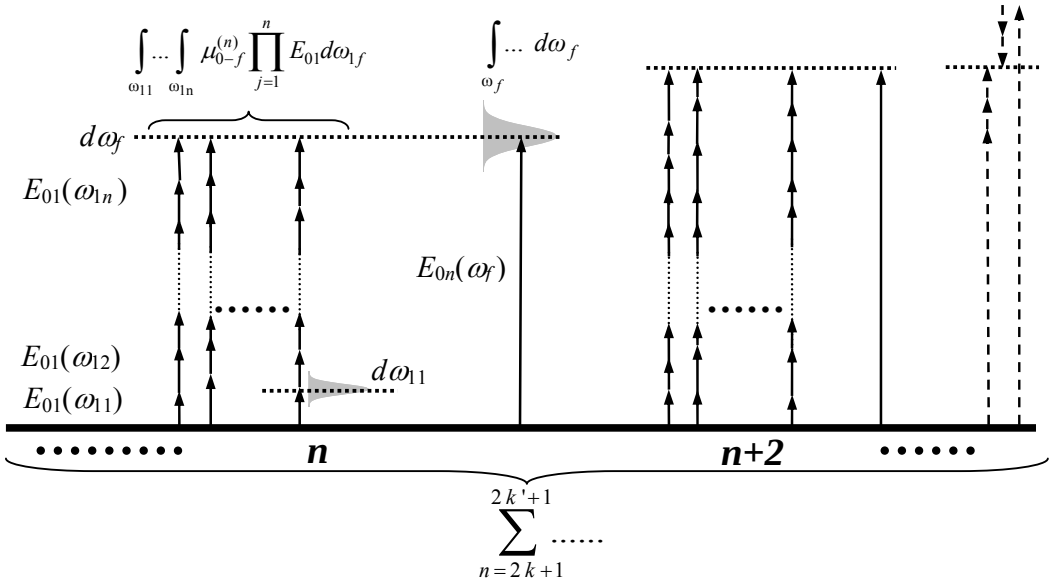

Figure 4.2: Scheme of the interfering channels leading to an excitation probability depending on the relative phase between the corresponding fundamental and the harmonic modes.

The amplitude of the total linearly polarized electric field of a superposition of the laser fundamental frequencies and that of its harmonics is given by

$$E(t)=\int_0^{\infty}\left(E_{01}(\omega)\exp\left[-i(\omega t-\varphi_1(\omega))\right]+\sum_{n=2k+1}^{2k'+1}E_{0n}(\omega)\exp\left[-i(\omega t-\varphi_n(\omega))\right]\right)d\omega\,, \quad (4.6)$$

where n denotes each harmonic, E_{01} and E_{0n} are the spectral amplitudes of the fundamental and of each harmonic, respectively, $\varphi_1(\omega)$ and $\varphi_n(\omega)$ correspond to the phases of the different spectral components and the sum is over all the odd harmonics with k and k' being integer numbers. When this field interacts with an atomic system, excitation takes place from an initial state $|0\rangle$ to the continuum or virtual final states $|f\rangle$. Now, using expressions of the lowest-order perturbation theory (LOPT) and of the electric dipole approximation, the excitation probability probed through harmonic emission is proportional to the square module of the sum of the n-photon excitation channels – through the appropriate combination of the n harmonic modes – and single-photon – through the n-th harmonic – transition amplitudes:

$$W_{0f}\propto\sum_{n=2k+1}^{2k'+1}\int_{\omega_f}\left|\int_{\omega_{11}}\int_{\omega_{12}}\cdots\int_{\omega_{1n}}\mu_{0-f}^{(n)}\prod_{j=1}^{n}E_{01}(\omega_{1j})\exp[i\varphi_1(\omega_{1j})]d\omega_{1j}+\right.$$

$$\left.+\,\mu_{0-f}^{(1)}E_{0n}(\omega_f)\exp[i\varphi_n(\omega_f)]\right|^2 d\omega_f\,, \quad (4.7)$$

where $\mu_{0-f}^{(n)}$ and $\mu_{0-f}^{(1)}$ are the corresponding n-photon and single-photon electric dipole moments of the transition between the initial state and the final states, respectively. The products $E_{01}(\omega_{11})E_{01}(\omega_{12})...E_{01}(\omega_{1n})$ refer to the n photons of the fundamental (i.e. n-photon transition) that couple the same initial and final state as the harmonic photon does, i.e. $\sum_{j=1}^{n}\omega_{1j}=\omega_f$. Equation (4.7) can be decomposed as follows:

$$W_{0f}\propto\sum_{n=2k+1}^{2k'+1}\int_{\omega_f}\left|\int_{\omega_{11}}\int_{\omega_{12}}\cdots\int_{\omega_{1n}}\mu_{0-f}^{(n)}\prod_{j=1}^{n}E_{01}(\omega_{1j})d\omega_{1j}\right|^2 d\omega_f+$$

$$+\int_{\omega_f}\left|\mu_{0-f}^{(1)}E_{0n}(\omega_f)\right|^2 d\omega_f+2\sum_{n=2k+1}^{2k'+1}\int_{\omega_f}\left(\int_{\omega_{11}}\int_{\omega_{12}}\cdots\int_{\omega_{1n}}\mu_{0-f}^{(n)}\prod_{j=1}^{n}E_{01}(\omega_{1j})d\omega_{1j}\right.$$

$$\times \mu_{0-f}^{(1)} E_{0n}(\omega_f)\Big) \cos\left(\varphi_n(\omega_f) - \sum_{j=1}^{n} \varphi_1(\omega_{1j})\right) d\omega_f \qquad (4.8)$$

From the last equation it can be clearly seen that the excitation probability oscillates as $\cos(\Delta\varphi)$, $\Delta\varphi = \varphi_n(\omega_f) - \sum_{j=1}^{n} \varphi_1(\omega_{1j})$ being the relative phase between the fundamental and the harmonics. This is expected since the interference in the present scheme occurs at the *n*-photon level.

By considering now Fourier-transform limited fundamental pulses i.e. the same initial phase $\varphi_1(\omega)$ within the spectral bandwidth, the phase difference for a given final state ω_f will be

$$\Delta\varphi = \varphi(\omega_f) - \sum_{j=1}^{n} \varphi(\omega_{1j}) = \varphi(\omega_f) - \sum_{j=1}^{n} \omega_{1j}\tau = \varphi(\omega_f) - \omega_f\tau\,, \qquad (4.9)$$

where τ is the variable delay between the fundamental and the harmonics. Therefore, the excitation probability and thus the measured quantity (e.g. the optical susceptibility) will depend only on the relative phase between the harmonic modes. Consequently, phase variations in each harmonic introduced through chirp can also be accounted. Having each harmonic component oscillating as $\cos(\varphi_n(\omega_f) - \omega_f\tau)$, summation over all components yields the temporal behavior of the coherent superposition of all harmonic modes involved.

4.3 Using the "phase-control" technique for the characterization of attosecond pulses

Temporal characterization of the XUV pulses requires the knowledge of their spectral phase and amplitude distribution. The "phase-control" of the excitation processes apart that aim to control the final products of the interaction can be used to probe the relative phase distribution between the fundamental and the harmonic modes, and thus the temporal characteristics of their superposition. The latter can be easily achieved by a Fourier transform of the eq. (4.8). Because of the different amplitude factors of the eqs.

(4.6) and (4.8), the variations of the excitation probability will not reflect to the total electric field as far as the amplitudes are concerned. Therefore, amplitudes have to be separately measured, for example, through conventional frequency domain spectroscopy (e.g. by using a monochromator to separately measure the spectral amplitudes of each harmonic). Alternatively, the determination of the total electric field would be possible by repeating the measurement selecting for each run a small frequency interval $d\omega$ of each harmonic and measuring simultaneously with their relative phase the field amplitude of this interval. Running for a few intervals within the bandwidth of one harmonic application of this approach allows for an evaluation of its chirp. Consequently, this treatment forms a versatile cross-correlation technique that can be used for the characterization of harmonics and thus of attosecond (XUV) pulses.

4.3.1 Numerical simulations

In this Section, we show some numerical simulations based on the perturbative expressions of the eqs. (4.6) and (4.8), in order to verify the temporal relation between these two equations that represent the total electric field and the measured excitation probability, respectively.

Let's consider a Gaussian pulse of which the spectral amplitude at a central frequency ω_j is given by

$$E_{0n}(\omega) = \exp\left[-\frac{1}{4}\tau_{Gn}^2(\omega-\omega_n)^2\right], \tag{4.10}$$

where $\tau_{Gn} = \tau_{pn} / \sqrt{2\ln 2}$ is the Gaussian width at the 1/e of the peak amplitude of the harmonic field n and τ_{pn} is the FWHM pulse duration of each harmonic n given by the expression (within the LOPT theory where $I_n = (I_1)^n$, I_1 being the intensity of the fundamental beam)

$$\tau_{p_n} = \frac{\tau_{p_1}}{\sqrt{n}}, \tag{4.11}$$

where τ_{p1} is the FWHM pulse duration of the fundamental [18]. From eq. (4.8) and eq. (4.10) and by considering $\int_{\omega_{11}}\int_{\omega_{12}}\ldots\int_{\omega_{1n}}\mu_{0-f}^{(n)}\prod_{j=1}^{n}E_{01}(\omega_{1j})\mu_{0-f}^{(1)}d\omega_{1j}$ being equal to unity – an assumption that is made in order to eliminate the unknown values of the electric dipole moments from these expressions – the excitation probability becomes

$$W_{0f}\propto C+\sum_{n=2k+1}^{2k'+1}\int_{\omega_f}\exp\left[-\frac{1}{4}\frac{\tau_{p_n}^2}{2\ln 2}\left(\omega-\omega_f\right)^2\right]\cos\left(\varphi_n(\omega_f)-\omega_f\tau\right)d\omega_f\ , \quad (4.12)$$

where C is a constant value that stands for the first two terms of the eq. (4.8).

For the numerical evaluations, a total electric field consisting of a Fourier-transform limited fundamental pulse and the superposition of the 11-15 odd harmonics has been considered. The fundamental electric field has a central wavelength of λ_L = 800 nm and a pulse duration of τ_p = 10-fs. Figure 4.3(a) shows the temporal harmonic electric field and 4.3(b) the excitation probability as a function of the delay with the fundamental pulse. Figures 4.3(c) and 4.3(d) depict the Fourier-transform spectrum and the spectral phase distribution of the excitation probability shown in Figure 4.3(b), respectively. For the numerical evaluation of this case, Fourier-transform limited harmonics have been considered leading to a zero phase distribution among the harmonic orders.

In Figures 4.4(a)-(c) a phase dependence proportional to ω^2 for the spectral modes of each harmonic (to account for the chirp within each harmonic) and between harmonics (to account for the chirp between harmonics) has been considered. In contrast with the preceding case, the linearly chirped harmonics are leading to an observable broadening of the excitation probability trace, exactly like the broadening in the total harmonic field. For the numerical evaluation, we have chosen a chirp value of 2-fs^2 that leads to a FWHM pulse duration of ~9.5-fs. The Fourier transform of the latter leads to the linearly chirped spectral phase distribution shown in Figure 4.4(d). It is worth noting that the produced phase distribution of the harmonic fields of interest stands for the phase distribution of the total electric field, since the fundamental electric field has a zero phase.

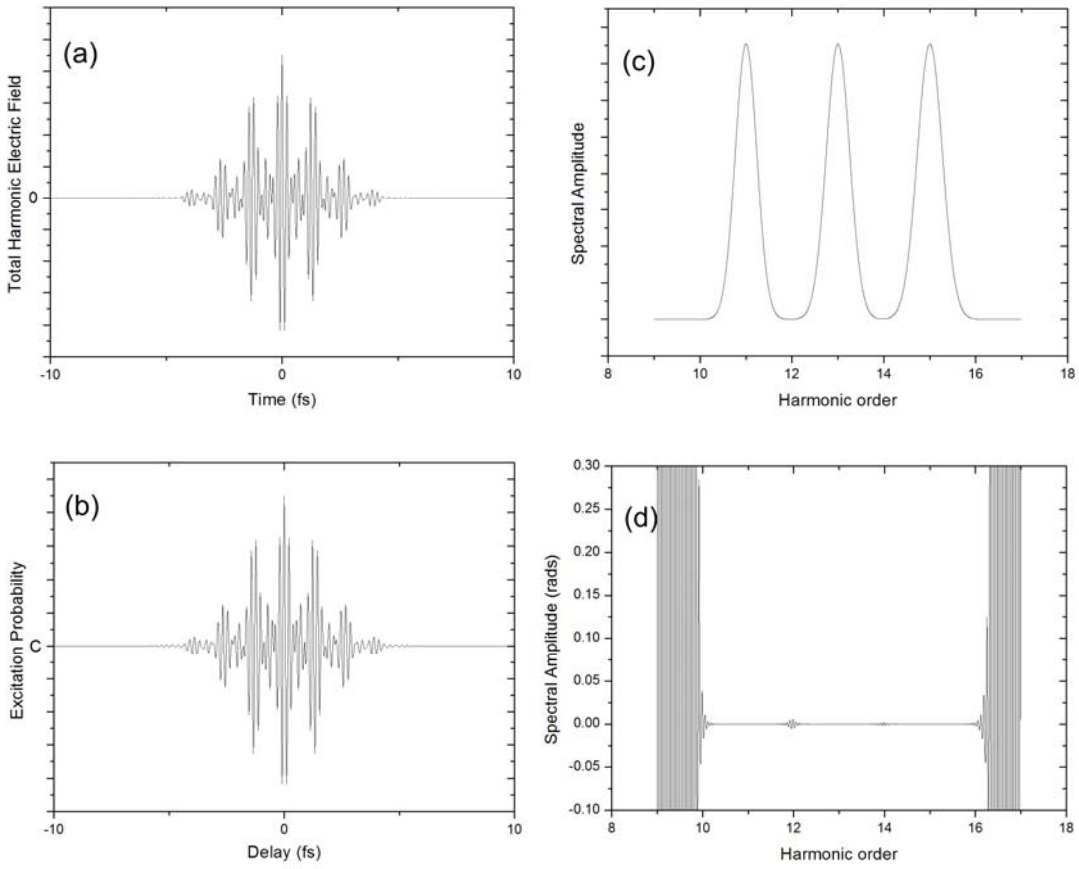

Figure 4.3: (a) Harmonic Electric field of the coherent superposition of 11 – 15 harmonics produced by a Gaussian Fourier-transform limited fundamental pulse of a 10-fs FWHM pulse-duration. (b) The excitation probability given by the eq. (4.12) as a function of the delay with the fundamental. (c) The spectral amplitude of the Fourier-transform of the excitation probability, and (d) the Fourier-transform spectral phase. The observed structure between the phases is due to numerical artifacts.

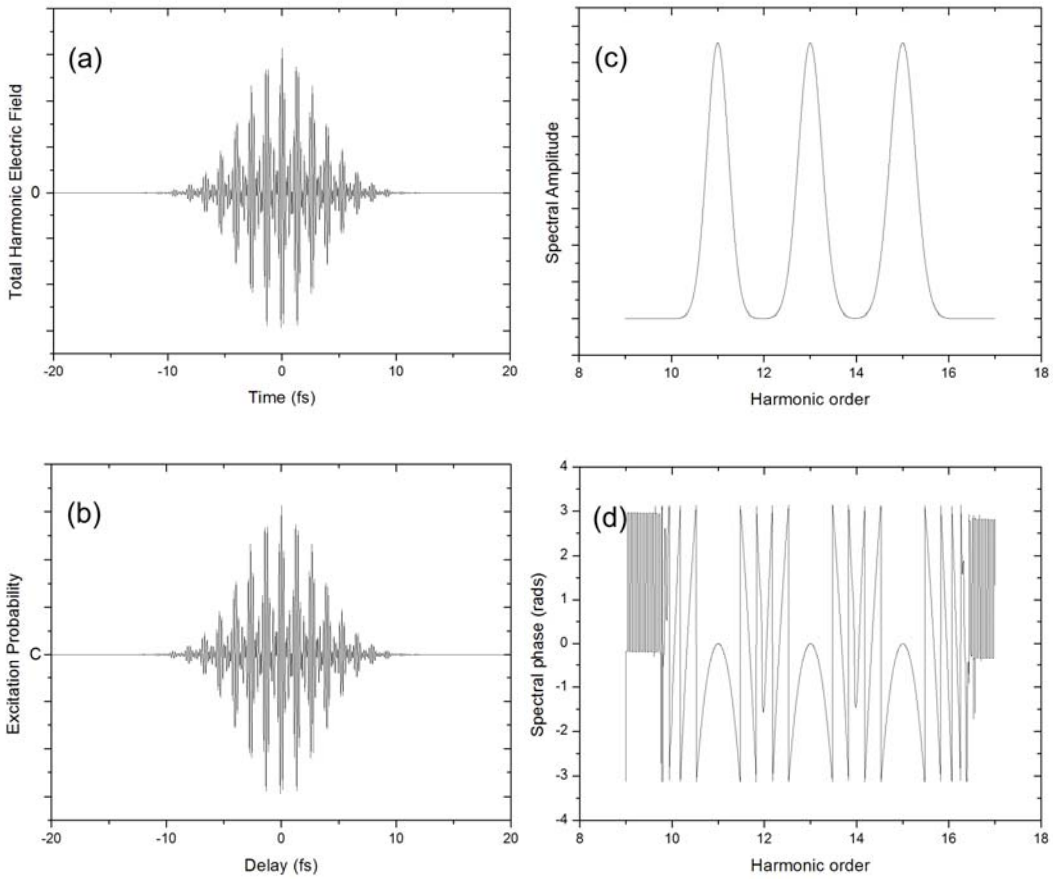

Figure 4.4: (a) The observed broadening of the total Harmonic Electric-field due to the introduced linear chirp within the harmonics and between the harmonics. (b) The excitation probability, (c) the spectral amplitude of the Fourier-transform of the excitation probability and (d) the Fourier-transform spectral phase shows the introduced linear chirp in the harmonics.

4.4 Using the phase-control technique for the characterization of a TH pulse

In this Section, we apply the previously described phase-control technique to the TH field (λ_3 = 267 nm) generated by a fundamental laser field with a central wavelength at 800 nm. This is to provide the theoretical framework upon which our experimental work is based on.

Consider the same atomic system used in our previous descriptions. In the case of the third harmonic generation (THG) the interfering channels of interest are depicted in Figure 4.5. The final state of the interaction is considered to be a virtual state of the atom. The total electric field, using the general expression (4.5), is given by

$$E(t) = \int_0^{\infty} \left(E_{01}(\omega) \exp\left[-i(\omega t - \varphi_1(\omega)) \right] + E_{03}(\omega) \exp\left[-i(\omega t - \varphi_3(\omega)) \right] \right) d\omega \,. \qquad (4.13)$$

where the assumption of linearly polarized electric fields consisting of the fundamental E_{01} and the corresponding TH modes has been considered.

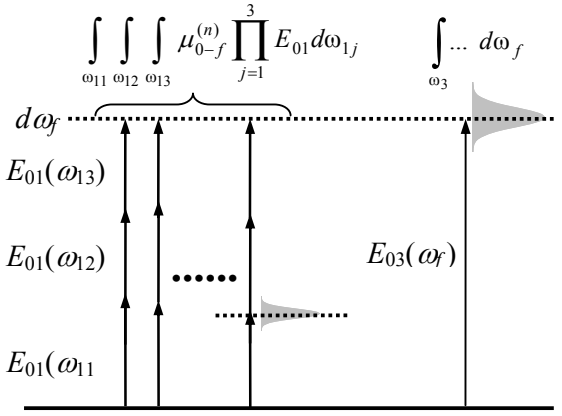

Figure 4.5: The interfering channels leading to an excitation probability depending on the relative phase between the corresponding fundamental and the third harmonic modes.

Interaction of this field with the atomic system leads to the excitation of the atoms. Thereby, the excitation probability is given by

$$W_{03} \propto C + 2\int_{\omega_3}\left(\int_{\omega_{11}}\int_{\omega_{12}}\int_{\omega_{13}}\mu_{03}^{(3)}\prod_{j=1}^{3}E_{01}(\omega_{1j})d\omega_{1j}\times\mu_{03}^{(1)}E_{03}(\omega_3)\right)\times$$
$$\times\cos\left(\varphi_3(\omega_3)-\omega_3\tau\right)d\omega_3, \qquad (4.14)$$

where ω_3 refers to the frequency of the TH and τ is the delay among these interfering channels. The last equation can be simplified by arbitrarily assuming $\int_{\omega_{11}}\int_{\omega_{12}}\int_{\omega_{13}}\mu_{03}^{(3)}\prod_{j=1}^{3}E_{01}(\omega_{1j})\mu_{03}^{(1)}d\omega_{1j}=1$, as this does not affect the phase factor and absolute values are not important. Equation (4.14) becomes

$$W_{03} \propto C + 2\int_{\omega_3}E_{03}(\omega_3)\cos\left(\varphi_3(\omega_3)-\omega_3\tau\right)d\omega_3\ . \qquad (4.15)$$

4.4.1 Numerical Simulations

By following the procedure of Section 4.3.1 numerical simulations of the excitation probability as given by the eq. (4.13), are presented. In this case, a Fourier-transform limited pulse having a carrier wavelength at 800-nm and pulse duration of 50-fs has been considered. Figures 4.6(a) and 4.6(b) depict the TH electric field and the excitation probability in the ideal case of a bandwidth limited TH pulse, respectively. Figures 4.6(c) and 4.6(d) show the Fourier transform spectral amplitude and spectral phase distribution, respectively.

In Figures 4.7(a)-(d) we show the results of the numerical evaluation for a linearly chirped TH pulse. The value of the chirp used is of 500-fs^2. The FWHM pulse duration of the TH Electric field broadens to about 90-fs. For the bandwidth-limited case, the FWHM pulse duration is ~35-fs according to the value predicted by the LOPT approximation.

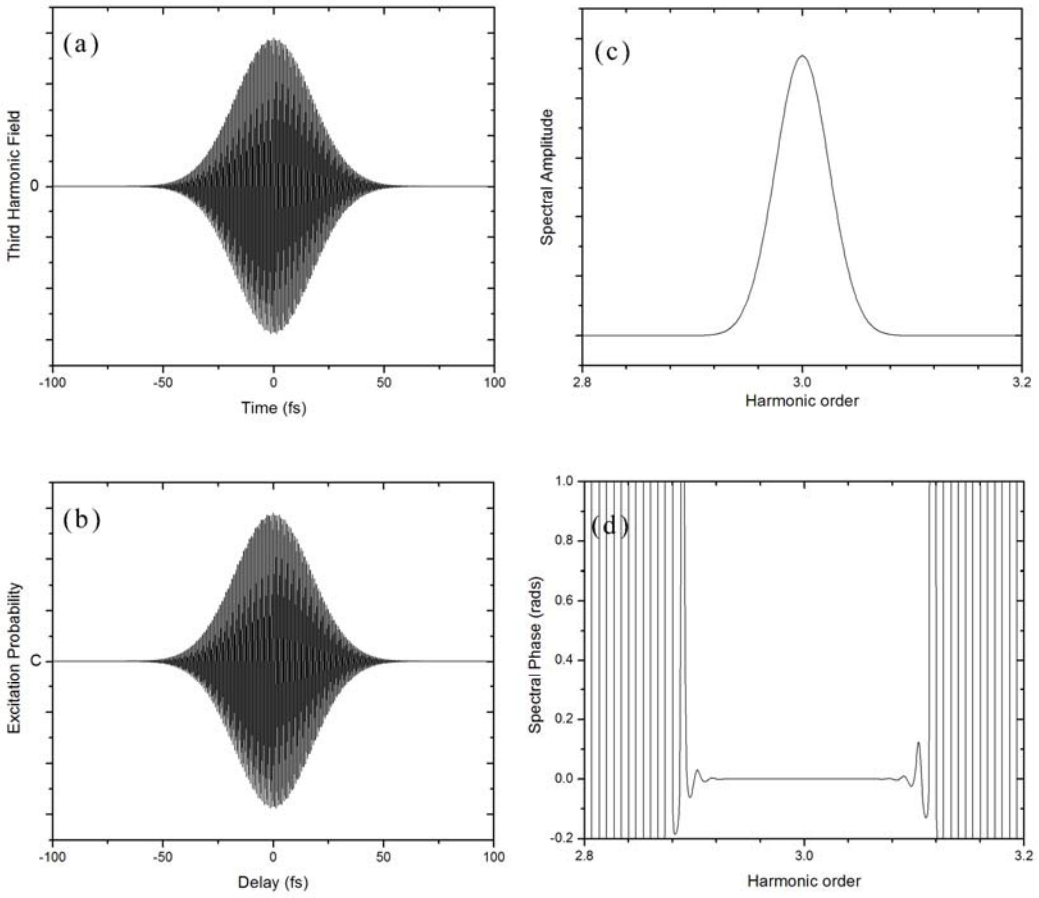

Figure 4.6: (a) The bandwidth limited Third Harmonic Electric field produced by a Gaussian Fourier-transform limited fundamental pulse of a 50-fs FWHM pulse duration. (b) The excitation probability as a function of the delay with the fundamental. (c) The spectral amplitude of the Fourier-transform of the excitation probability, and (d) the spectral phase distribution across the TH peak.

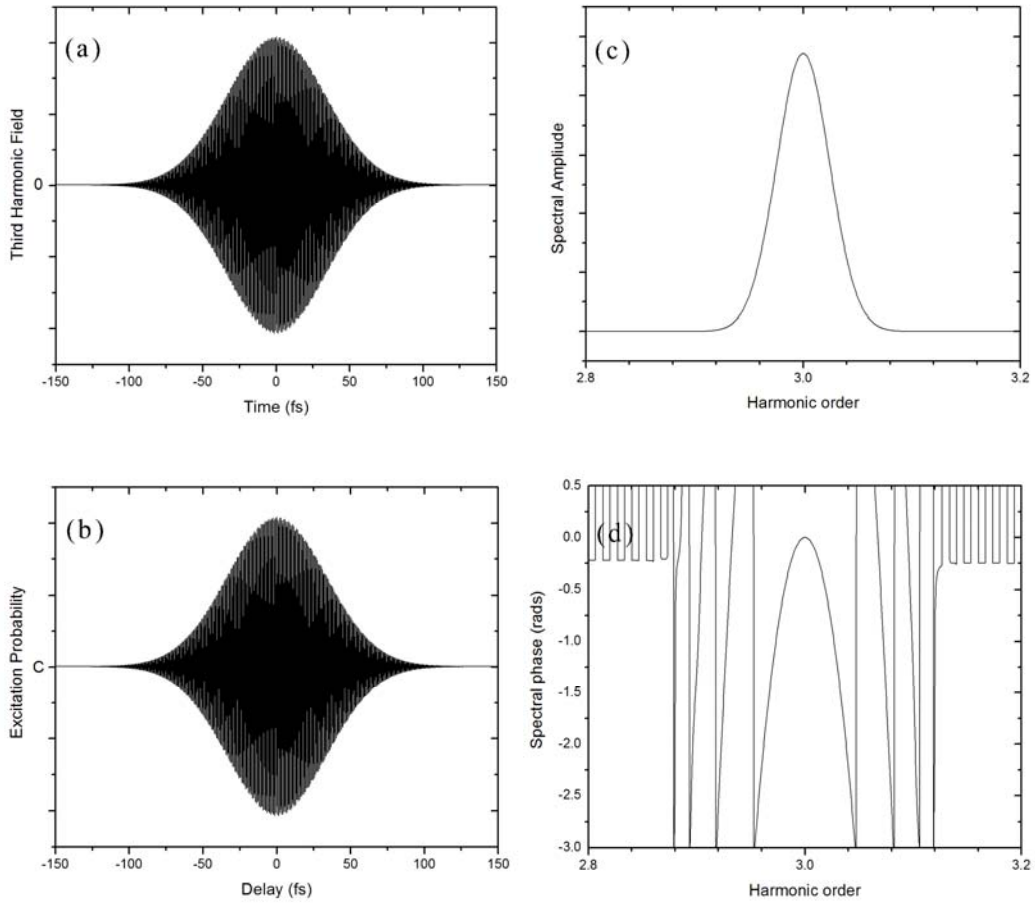

Figure 4.7: (a) The linearly chirped third harmonic electric field produced by a Gaussian Fourier-limited fundamental pulse of 50-fs FWHM pulse duration. (b) The excitation probability given by the eq. (4.13) as a function of the delay with the fundamental. (c) The spectral amplitude of the Fourier-transform of the excitation probability, and (d) the Fourier-transform spectral phase distribution showing the chirp within the pulse.

In both cases it is well observable that the excitation probability traces are broadening in time as the total harmonic field does. The spectral amplitudes should not be affected by the introduced chirp, as is the case of the above results. In principle, this is what is expected from a cross-correlation measurement performed with a dispersionless apparatus.

Chapter 5

Characterization of the TH by using the Transmission Grating Interferometer

5.1 Introduction

For the implementation of the method described in the preceding Chapter, a dispersionless experimental arrangement is required. Such an arrangement has already been proposed [1] and theoretically investigated [2]. The main concept is based on utilizing a freestanding transmission grating as a beam-splitter in a Michelson-like interferometer for the spectral separation of the involved harmonics. This provides the possibility for the selection of a group or individual harmonics and temporally cross-correlate them/it with the fundamental pulse. This interferometer comprises the experimental arrangement used for the temporal characterization of the TH pulse generated by a Ti:Sapphire laser, presented in this Chapter.

In particular, in Section 5.2, the general properties and the basic optical configuration of interferometric arrangements based on a freestanding transmission grating are outlined. In Section 5.3 the optical configuration of the used arrangement is specified. In Section 5.4 a ray-tracing study for the TH wavelength and the optical set-up used is presented and its dispersionless operation is established. Section 5.5 describes the experimental details. Section 5.6 presents and discuses the obtained experimental results. Finally, Section 5.7, summarizes our findings.

5.2 The Transmission Grating Interferometer (TGI)

The principle of the transmission grating interferometer is depicted in Figure 5.1 and is comprised to that of a conventional Michelson one. A freestanding transmission grating provides the possibility to split the incident beam into one zeroth-order and two diffracted first-orders. Two spherical mirrors reflect the zeroth-order and one of the two first-orders back to the grating and by passing through it, the first-order of the primary zeroth-order and the zeroth-order of the primary first-order recombine and co-propagate towards a third spherical mirror, which reflects and focuses both beams on the detector. Each optical component of this configuration plays a crucial role to the extension of the interferometer in the XUV spectral regime and to its dispersionless characteristics, making it an ideal tool for the characterization of attosecond pulses. In the following the purpose of each component is discussed.

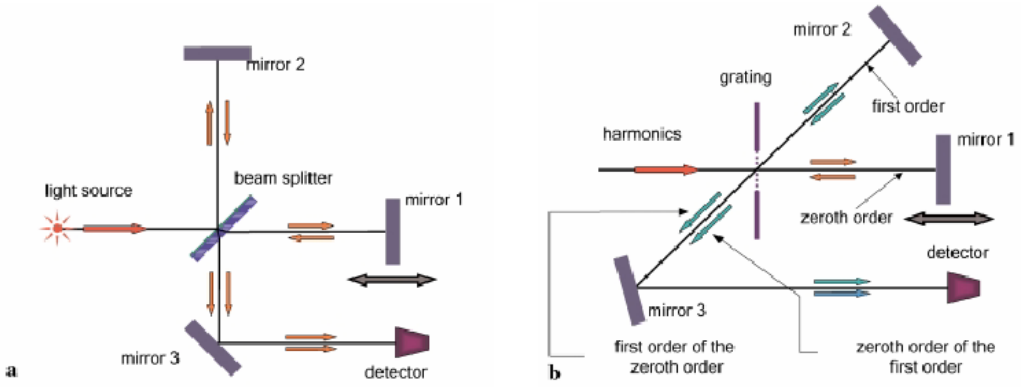

Figure 5.1: (a) the conventional Michelson interferometer which can be used in order to characterize femtosecond pulses in auto-correlation techniques and (b) the freestanding grating based interferometer, which can be used to extend the characterization to the XUV spectral regime (E. Goulielmakis *et al*. 2002)

First of all, the replacement of the beam-splitter by a freestanding transmission grating is for a few but rather important purposes. Nowadays technology provides the possibility to use special dielectric-coated beam-splitters in the infrared (IR) and visible

spectral regime with minimum dispersion by minimizing the thickness to a few microns (i.e. pellicle). Although this sounds optimistic the option of using something similar in the XUV regime is precluded, since all the materials are opaque to this radiation. On the other hand, although reflection gratings have already been used in such interferometers [4], their extension to the XUV is unequivocally far beyond of any hope, since their efficiency varies strongly with the wavelength. The use of a transmission grating exhibits an additional feature. It spectrally analyzes the incident radiation of gas-harmonics. The spectrum is discrete and the isolation of one harmonic or a group of harmonics can be easily implemented (e.g. by simply introducing obstacles). Furthermore, such a grating has a constant efficiency for all the wavelengths of interest providing an advantage over the reflection-based one. Additional properties and construction characteristics are provided in Ref. [2].

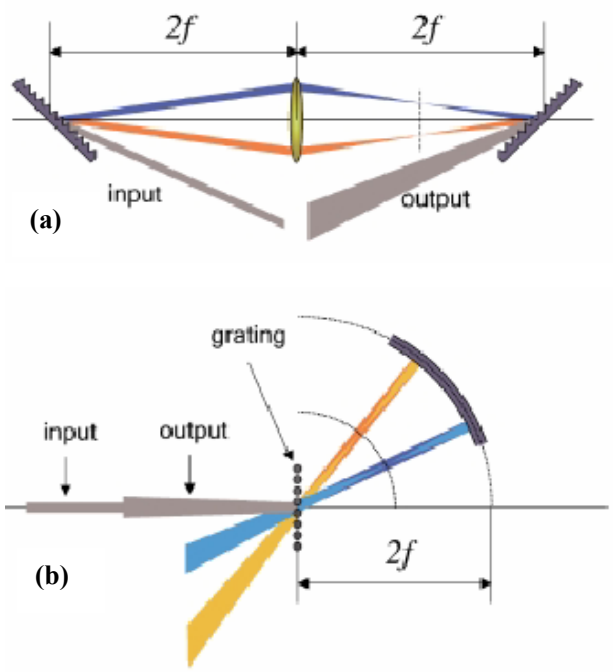

Figure 5.2: (a) a zero-dispersion arrangement consisting of two reflection gratings and a single lens positioned in such a way as to obtain a direct image of each grating into the other. (b) A dispersionless Michelson-like interferometer consisting of one transmission grating and one spherical mirror. The transmission grating plays the role of the two reflection gratings and the spherical mirror that of the lens (E. Goulielmakis *et al.* 2002).

The next step is to replace the, so used in conventional interferometers, flat mirrors with spherical ones. Spherical mirrors are considered to be free of chromatic aberrations for in-axis propagation, providing the advantage of maintaining a dispersionless configuration. Additionally, by placing the mirrors in such a position as to image the grating into itself (see Figure 5.2), the dispersion introduced by the grating can be eliminated. This method, actually, resembles to a zero-dispersion-pulse-compressor arrangement used for shaping femtosecond pulses.

Although the introduction of the third spherical mirror seems to be useful only in focusing both co-propagating beams on the detector, its role appears decisive in reducing the overall dispersion introduced by the interferometer, to acceptable limits. Finally, a non-linear medium is required for the generation of the harmonics and another one for their detection.

The applicability of this configuration has already been studied by E. Goulielmakis *et al*. Ray-tracing calculations for three different geometries detailed the operational characteristics of the set-up. In the first geometry the two spherical mirrors of the interferometer have been placed in such a way as to have their foci at the middle of the grating while the third mirror is positioned so that the grating is imaged into the detector plane. The results from the ray-tracing calculations reveal an extremely low-dispersion behavior of the order of one attosecond. Although all the harmonics, irrespectively of the arm that they belong to, have the same spot-size on the detector plane, the overall focal spot-size exceeds the limit of tight-focusing and that is due to the magnification factor introduced by the third spherical mirror. Subsequently, this geometry is useful only for field-correlation measurements. In the second geometry, instead of imaging the grating on the detector plane, the harmonic source is imaged on the detector. Therefore, both mirrors, after diffraction of the beams from the grating, form an image of the source in a position between mirrors and grating having all the harmonics locating in a concentric circle (Figure 5.3). Although this reduces the overall focal spot-size on the detector plane, it suffers from slight dispersion of less than 1-fs.

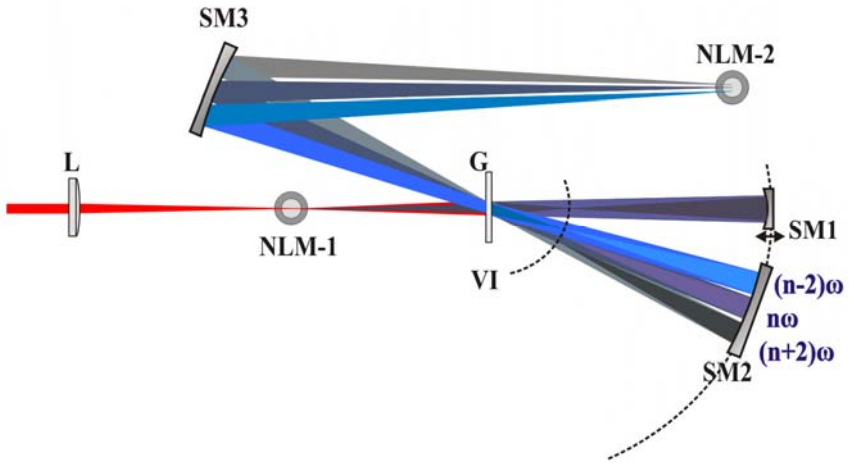

Figure 5.3: Optical paths of the harmonics $(n+2)\omega$, $n\omega$ and $(n-2)\omega$ for both arms (zero-first and first-zero orders) for the geometry of case II in Ref. [2]. L denotes the lens used to focus the fundamental into the harmonic source medium NLM-1. G denotes the grating, SM1, SM2 and SM3 the spherical mirrors and VI the between-image of the interaction region in NLM-1 and the detector plane NLM-2.

Both optical arrangements have been already used for the characterization of femtosecond duration pulses by second order AC and intensity AC measurements [3]. Particularly, they have been used in order to characterize the simple case of the third harmonic produced in a gas medium. The results showed to be in agreement with those carried out with a conventional Michelson interferometer.

An alternative approach that combines the advantages of the two above geometries has also been proposed as case III by E. Goulielmakis *et al.* (2002). This configuration is appropriate for cross-correlation measurements and possesses all the necessary prerequisites for the characterization of higher-order harmonics and ultra-short pulses.

5.3 A Transmission Grating Interferometer for the characterization of high order harmonics

The geometry by which the transmission grating interferometer can be used for the characterization of high-order harmonics is depicted in Figure 5.4. The co-propagating fundamental and the harmonic beams generated in a non-linear medium, e.g. a gas-jet (NLM-1), impinge on a freestanding transmission grating and they are spectrally dispersed The zeroth-order passes straight through while the harmonics diffract in the two first-orders. The selection of the harmonics of interest can be implemented by using the appropriate obstacles (e.g. spatial filters or diaphragms). The reflected back to the grating orders from the spherical mirrors (SM1 and SM2) are slightly elevated in the vertical plane and thus spatially separated from the primary incoming beams. Consequently, the elevation of the beams affects slightly the between-image of the interaction region (NLM-1) located on a concentric circle having a distance $s < r_{SM2}/2$ from the grating, where r_{SM2} is the corresponding radius of the mirror SM2 (the same distance stands for the case of the between-image in the arm of the spherical mirror SM1). One arm comprises of the zeroth-zeroth-order path and the other of the first-first-order path. This results in reducing the overall efficiency to ~1%. Considering this fact, this could be an important disadvantage for measuring high-order harmonics and this is due to their characteristic low intensity.

Exiting the grating all the first orders of the selected harmonics are co-propagating with the zeroth-zeroth-order of the fundamental to the third spherical mirror (SM3) that focuses the beams to a second non-linear medium (NLM-2). This mirror images the between-image of the interaction region (NLM-1) in the second non-linear medium. By placing on the mirror SM1 on translation stage it is possible to temporally delay the fundamental with respect to the harmonics produced in the NLM-1, thus monitoring the harmonics generated in the NLM-2 as a function of the delay. Consequently, a cross-correlation trace can be recorded that carries all the information of the spectral phase distribution.

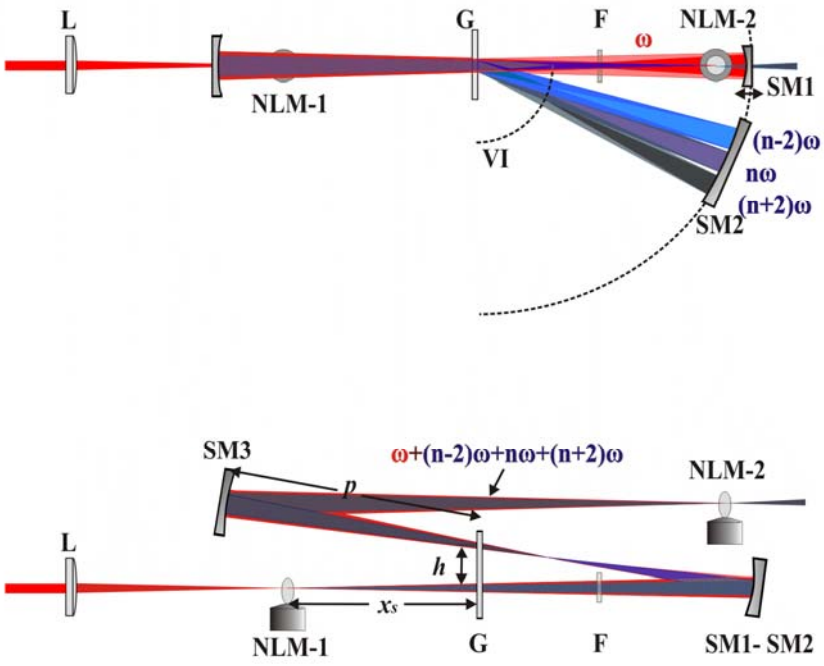

Figure 5.4: Schematic layout of a 3D grating interferometer. *Top:* A top view and *Bottom:* a side view. The slight tilting of spherical mirrors SM1, SM2 and SM3 gives rise to an elevation *h* at the grating G between incident and retro-reflected beams. Each of the dispersed harmonics forms an image of their generation region NLM-1 that lies on the circumference of a circle VI with center at the middle of the grating. This image is further relayed to an interaction region NLM-2 where the cross-correlation takes place. The harmonics are filtered out from the zeroth order by means of a filter F (E. Goulielmakis *et al.* 2002)

A 3D ray-tracing code applied to this configuration showed, for three values of elevation *h*, a negligible deviation from a dispersionless operation [2]. Therefore, both requirements for low-dispersion and tight-focusing are satisfied simultaneously making this layout the appropriate interferometer for experimental measurements in the XUV regime.

On the other hand, although the applicability of this arrangement theoretically has been proven, experimentally has not yet been investigated. The utilization of this interferometer for the characterization of the simple case of the third harmonic field of

a Ti:Sapphire laser generated in a gas medium, is the subject of discussion of the next Sections.

5.4 The TGI for the case of the TH pulse

5.4.1 Introduction

This Section investigates the simplest case of a cross-correlation measurement using the transmission grating interferometer. The cross-correlation is between the TH generated in a gas medium and the fundamental Ti:Sapphire laser beam. We used the TH, the lowest harmonic order, in a proof of the principle manner. Prior to the experiment, a 3D ray-tracing analysis for the propagation of the TH-beam through the interferometric set-up, via which predictions on aberrations and dispersion, has been performed.

5.4.2 3D ray-tracing analysis

In this Section we present the 3D ray-tracing analysis for the TH wavelength in the geometry used in performing the experiment. For the 3D ray-tracing the 3D capabilities of the OPTICA® package of Mathematica® has been used.

The 3D ray-tracing code is of particular importance in analyzing this set-up, since it can account for the effects of the beam propagation through the grating and the tilted mirrors on the dispersion and focusing characteristics. Furthermore, it assesses the geometric aberrations due to the optical elements of choice and the geometry used. Consequently, we present results of the paraxial group-delay and the group-delay dispersion (GDD) as a function of the frequency for five different values of the elevation h on the grating surface. This ray-tracing evaluation has been carried out for a certain value of the distance between the third spherical mirror SM3 and the grating G, as well as for two gratings with different number of grooves/mm. All the parameters and values used for the calculations are given in Table 5.1. It is worth noting that in

order to evaluate the group-delay and the group-delay dispersion, a light ray that travels through a dispersive element as a function of the frequency components (modes) of the pulse has been considered. Therefore, once the optical path difference of the extreme paraxial ray from the chief (central) ray as a function of frequency has been determined, the group-delay is equal to $\Delta t_{front}(\omega) = \max(l_{paraxial}(\omega) - l_{chief}(\omega))/c$ and the group-delay dispersion of a short pulse is given by

$$D_2 = \frac{1}{c}\frac{dl_{front}(\omega)}{d\omega} = \frac{dt_{front}(\omega)}{d\omega}, \tag{5.1}$$

where $l_{front}(\omega)$ is the frequency dependent optical path, $\Delta t_{front}(\omega)$ is the difference in the arrival times between the chief-ray and the extreme paraxial ray of the TH and c is the speed of the light in vacuum.

Parameters	**Configuration I**	**Configuration II**
λ_L (nm)	800	800
λ_3 (nm)	266	266
$N_{Grating}$ (l/mm)	300	600
x_s (mm)	250	250
R_{SM1} (mm)	300	300
R_{SM2} (mm)	300	300
R_{SM3} (mm)	300	300
θ_{SM3} (deg)	~ 4.57	~ 9.18
x_{SM3}† (mm)	170	170
h (mm)	1, 3, 5, 8, 10	1, 3, 5, 8, 10

† is defined as $x_{SM3} = p\cos(\varphi)$, where φ is the elevation angle.

Table 5.1: All the parameters and values used in performing the 3D ray-tracing calculations.

The ray-tracing results for the TH wavelength are summarized in Figures 5.5. In particular, Figures 5.4(a) and (b) show the results of the configuration I, , while Figures 5.4(c) and (d) depict the results for the configuration II. In both configurations a Fourier-transform limited Gaussian TH pulse has been considered. As it is expected,

the 300-lines/mm grating introduces less GDD to the pulse compared to the 600-lines/mm grating with increasing elevation height *h*. This is due to the difference in dispersive angles, which in the first configuration is shorter than the second one [5]. More important though is the fact that both configurations have showed negligible dispersion characteristics and thus they are both suitable for the experiment.

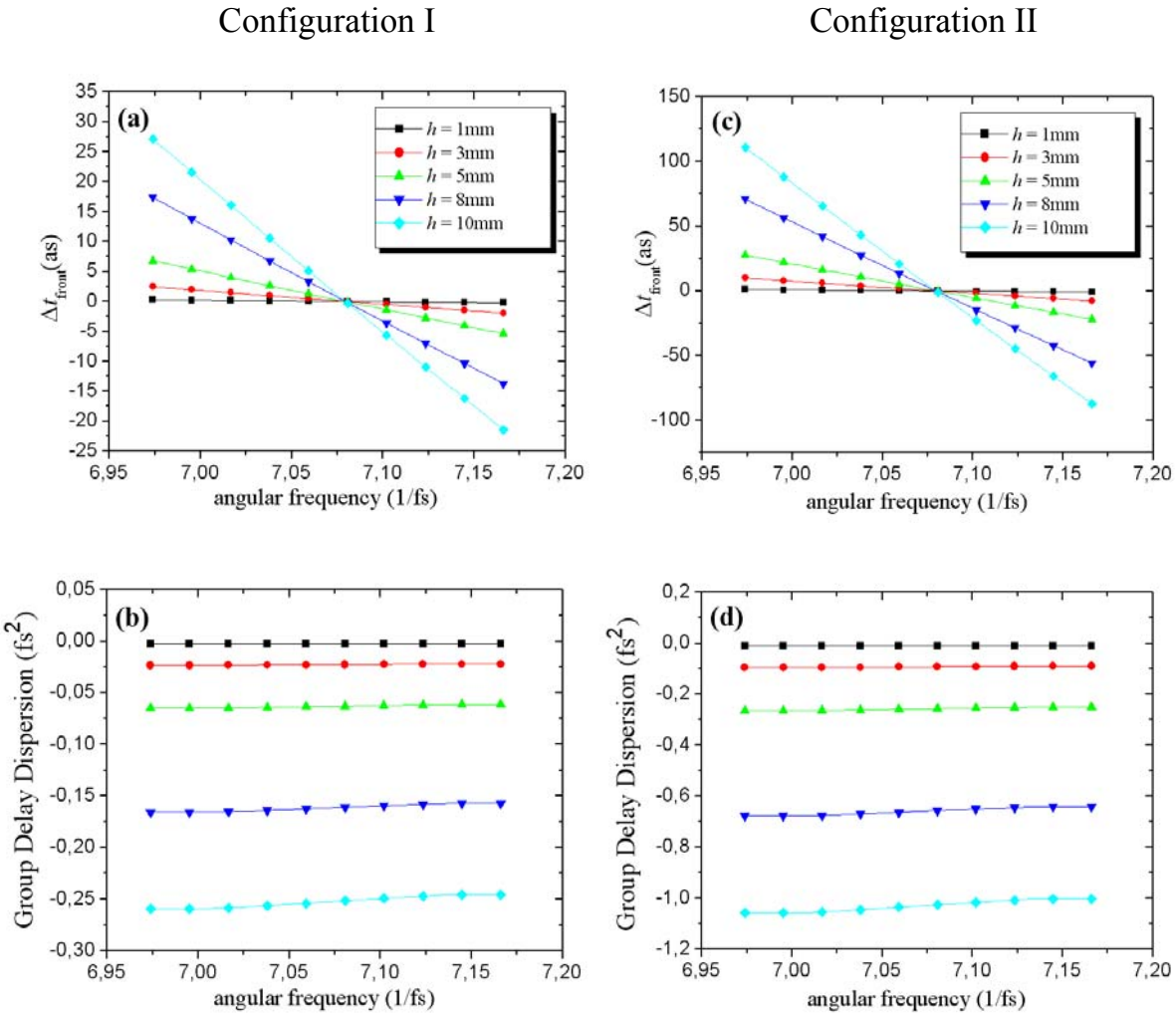

Figure 5.5: Ray-tracing results of the TH for the indicated elevation values of the inset legend and for the case of two gratings of different number of grooves per unit length. The Figures (a) and (b) correspond to a grating of 300-lines/mm, while the Figures (c) and (d) to a grating of 600-lines/mm. (a) and (c) depict the group-delay from the central angular frequency of ω_3 = 7.08 1/fs and (b) and (d) the group-delay dispersion obtained by differentiation of the smooth spline-interpolation of the group-delay (a).

Figure 5.6(a) and (b) show the results, from the ray-tracing code, of the TH beam propagated within the confocal parameter of the NLM-2 in the case of a 600-lines/mm and a 300-lines/mm grating, respectively. The scaled axis on the bottom presents the beam propagation axis within the confocal parameter. Each picture shows a cross-section of the TH beam while dots depict geometric rays on this cross-section. The observed astigmatism results from the slightly tilted spherical mirrors, which in the configuration I it leads to a larger focal-spot than that of the configuration II. The smallest focal-spot found for the case of 600-lines/mm grating is ~57-μm and the focal-spot found for the case of 300-lines/mm grating is ~19-μm.

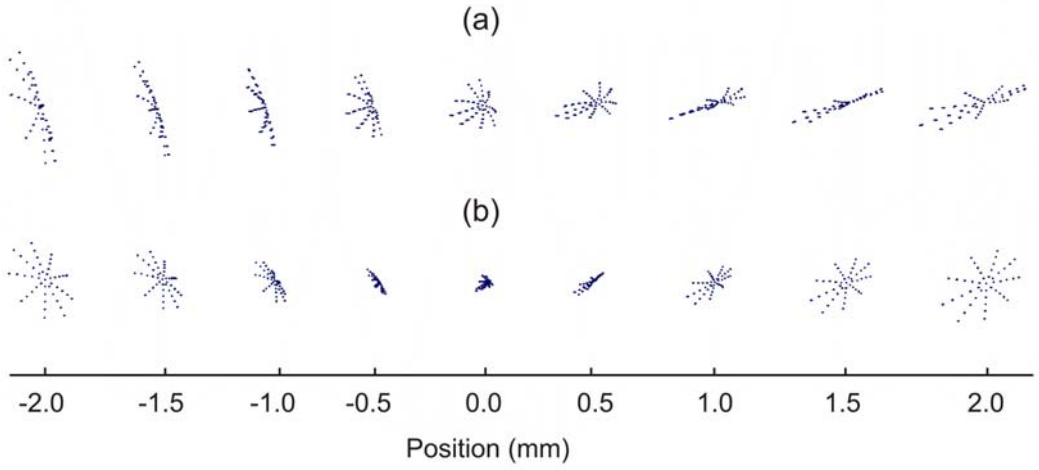

Figure 5.6: The observed astigmatism of the TH within the confocal parameter of the NLM-2 as a result of the ray-tracing analysis performed with the OPTICA® package of Mathematica®. Each picture depicts a cross-section of the TH beam while dots depict geometric rays on the cross-section. (a) The case of a 600-lines/mm grating and (b) the case of a 300-lines/mm grating.

5.5. Experimental

5.5.1 The femtosecond Ti:Sapphire Laser system

All the experimental work of this thesis was carried out using the femtosecond Ti:Sapphire amplified laser system at the Ultraviolet Laser Facility (U.L.F.) of the I.E.S.L – F.O.R.T.H. A schematic layout of the complete laser system is depicted in Figure 5.7. It comprises of a commercial Mira and B.M. Industries laser system using a combination of a Mira master oscillator, a pulse stretcher, a 1-kHz two-stage amplification configuration and a pulse compressor.

The oscillator, which is a Ti:Sapphire laser, based on a Kerr lens mode-locking configuration, is pumped by a CW diode laser (VERDI COHERENT) at 532-nm with 5 W average power and it generates pulses of ~ 25-fs at a wavelength of about 800-nm, having a pulse energy of ~ 5-nJ.

The generated pulses are stretched up to about 1000-5000 times their initial temporal duration in order to prevent optical damage because of the extremely high intensity, before is seeded into the amplification stages.

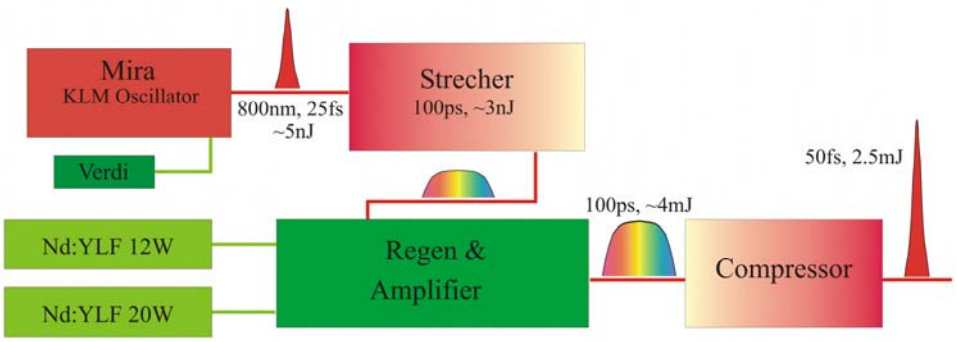

Figure 5.7: A schematic layout of the pulse amplification stages of the Ti:Sapphire laser system.

The first amplification stage is a regenerative amplifier, where selected seeding pulses are trapped in using Pockels cell based polarization switching. The active medium used for the amplification is a Ti:Sapphire pumped by a doubled frequency Nd:YLF (532-nm) at 12 W. The pulses are amplified having an energy of ~1.5 mJ/pulse and a 1-kHz repetition rate. The second amplification stage is a multi-pass amplified configuration, using a Ti:Sapphire crystal as an active medium pumped by a doubled frequency Nd:YLF (532-nm) at 20 W. The pulses are amplified reaching an energy of ~4 mJ/pulse.

Finally, the pulses are compressed using a grating-tandem compressor to a system pulse-width of 50-fs assuming a Gaussian pulse profile. The energy reaches the ~2.5 mJ/pulse.

The spectral and temporal profiles of the nearly Fourier-transform limited amplified laser pulse are shown in Figure 5.8. The profiles have been measured with a commercial SPIDER (Spectral Phase Interferometer for Direct Electric-field Reconstruction) apparatus available by APE. The temporal width of the pulse is measured to be 56 ± 4 fs having a carrier wavelength at 803-nm.

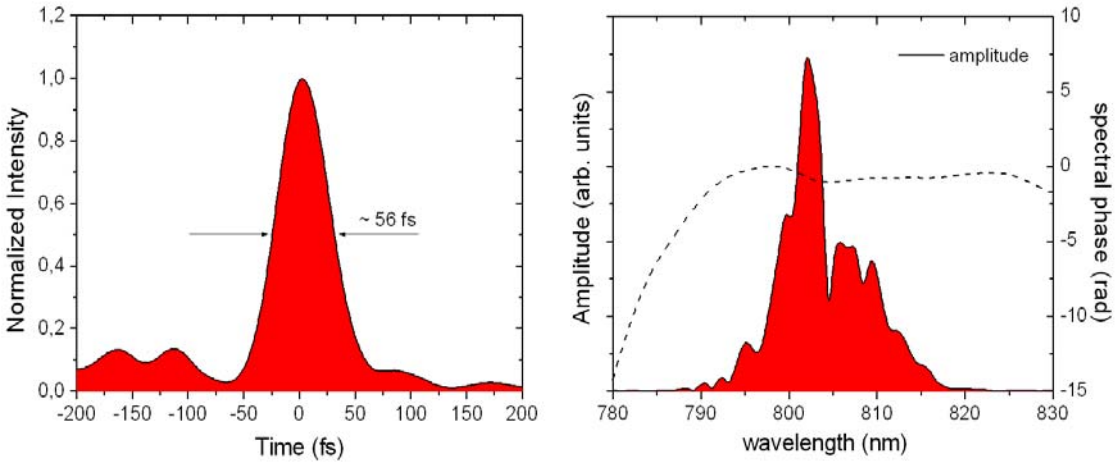

Figure 5.8: *Left:* The temporal and *Right:* the spectral profile of the pulse from the amplified Ti:Sapphire laser system measured with a commercial SPIDER instrument available by APE. The dotted curve in the right figure represents the measured spectral phase. The almost flat spectral phase across the pulse indicates for a nearly Fourier-limited pulse.

5.5.2 Optical layout

The experimental optical layout is depicted in Figure 5.9. The laser beam is focused by a 30-cm focal length planoconvex-lens into a 10-cm-long static cell filled with Xe in which harmonic generation takes place. A 0.5-mm of diameter pinhole is placed directly at the exit of the gas-cell. The later is utilized for the separation of the gas-cell from the vacuum chamber. In addition, by focusing the beam slightly after the pinhole the THG signal is maximized. The fundamental and the generated third harmonic are entering into the vacuum chamber where the described grating-interferometer is built in. The beams are spectrally dispersed by a 1-mm-thick fused silica transmission grating of 600-lines/mm optimized for maximum throughput at 266-nm. The zeroth-order of the fundamental pulse passes through a 1-mm-thick BK7 glass in order to filter out the zeroth-order TH and impinges on a 30-cm radius of curvature Au-coated spherical mirror (SM1) mounted on a stepper-motor controlled delay-stage. The first-order of the spectrally dispersed TH impinges on a second 30-cm radius of curvature Au-coated spherical mirror (SM2). The diffraction angle has been calculated to be ~9.18^{o}. Both mirrors are tilted by ~2^{o} and the retro-reflected beams are sent back to the grating having an elevation height of ~10mm. The zeroth-zeroth-order of the fundamental and the first-first-order of the TH are focused into a second 10-cm-long static cell by the third 30-cm radius of curvature Al-coated spherical mirror (SM3). The mirror SM3 is located in a distance of 170mm from the grating. The gas-cell is of cylindrical shape with a diameter of ~25-mm and is filled with Xe gas. A schematic picture of the interaction region in the cell, where the two pulses are interfering, is shown in Figure 5.10. Their interference as a function of the delay is recorded at the exit of the vacuum chamber.

The main alignment requirement in this set-up is to spatially overlap the zeroth-order of the fundamental and the first-order of the TH, simultaneously on the grating surface and into the interaction region of the second static cell (NLM-2). This is in order to ensure their co-propagation from the grating to the detector. The total optical path-length that both beams are traveling through the interferometer is 60-cm. A lens of 2-m focal length is placed outside of the vacuum chamber after the second static cell (NLM-2), such as to image the interaction region (NLM-2) in a distance of ~5-m away from the lens by simultaneously magnifying the foci of the two beams. The latter

comprises an important fine alignment tool when the chamber is under vacuum. In addition, the spherical mirror SM2 is mounted on a two-dimensional (θ-φ) pico-motor control unit giving the possibility of being remotely controlled.

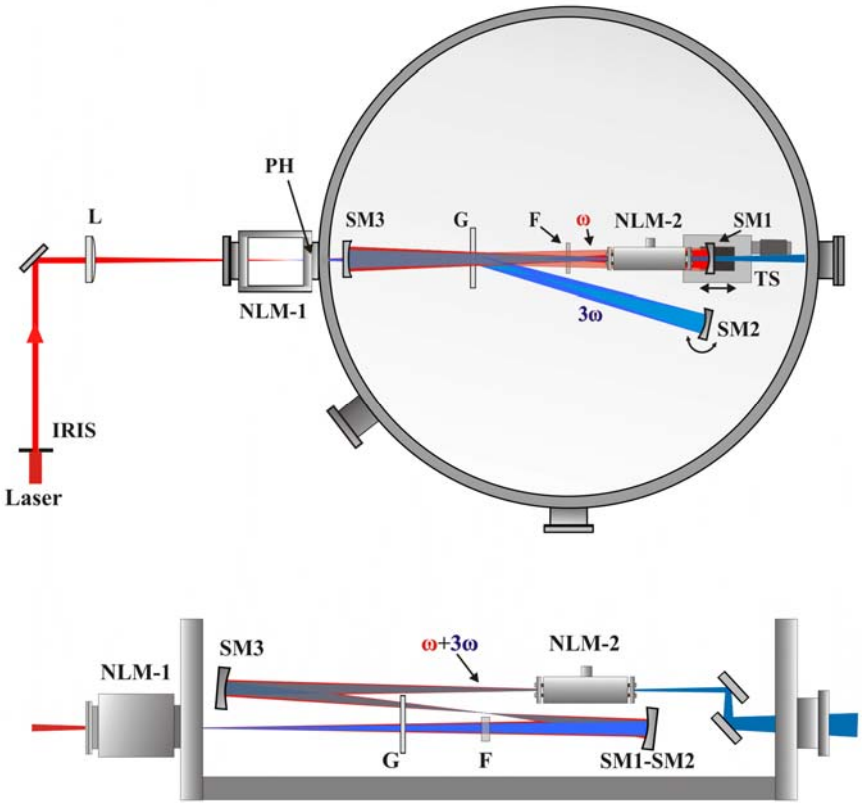

Figure 5.9: A schematic optical layout of the experimental set-up. *Top:* a top view and *Bottom:* a side view. The fundamental beam from the Ti:Sapphire laser system after passed through an aperture IRIS is focused into NLM-1 by a f = 30-cm lens L. The generated TH and the fundamental enter into the vacuum chamber after passed though a pinhole PH and impinge onto the 600-lines/mm grating G. The spectrally dispersed first-order TH is reflected back to the grating by the mirror SM2 slightly elevated in the vertical axis. The zeroth-order TH is filtered out by a 1-mm-thick BK7 glass F and thus only the fundamental beam is reflected back to the grating by the spherical mirror SM1. The SM1 is mounted on a translation stage TS. Both, the fundamental and the TH are focused into the NLM-2 by the mirror SM3.

For the fine alignment procedure, when the chamber is under vacuum conditions, the two generated TH pulses are spatially overlapped outside the chamber. This can be easily accomplished by looking far away the image of their focus and by fine adjusting their relative position using the pico-motorized mirror SM2. Their spatio-temporal interference can be achieved by finding the zero-delay of the two overlapping pulses. In addition, the observation of a single spatial interferometric fringe indicates the existence of two co-propagating and interfering pulses after their recombination at the grating.

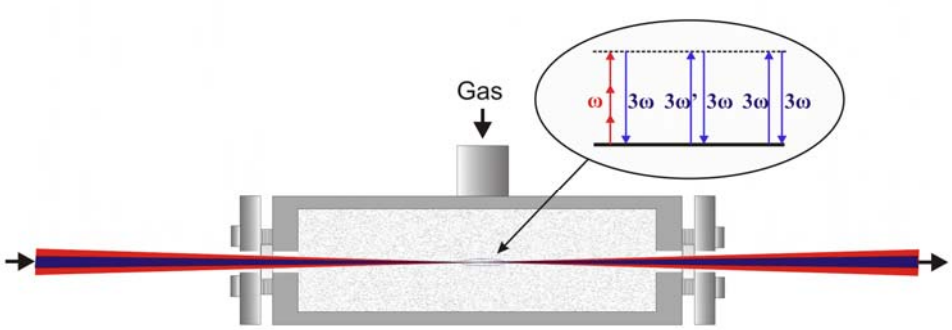

Figure 5.10: The interaction region in the second static gas-cell where interference between the different excitation channels takes place. The gas-cell has a pair of 3mm-thick LiF windows as to allow the transmission of the UV radiation.

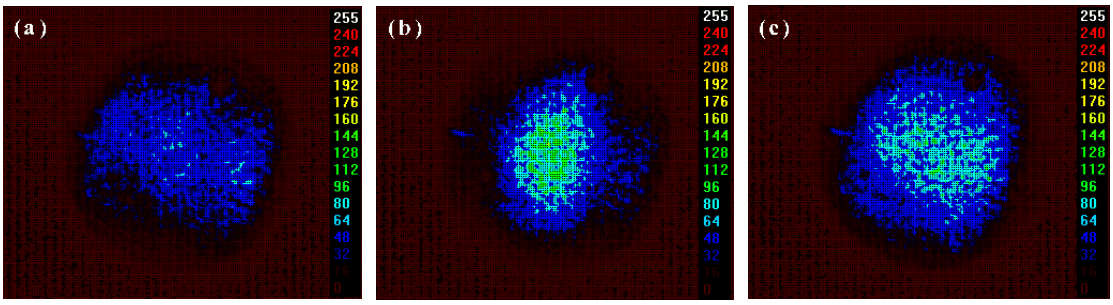

Figure 5.11: Spatial interference fringes of the TH recorded for three different delays between the two overlapping pulses. The images are captured by a CCD camera placed after mirror SM3 at the exit of the vacuum chamber. The mirror SM3 eliminates the shifting of the fringes due to the relative tilt of the pulse fronts.

Figures 5.11 depict the almost single spatial interfering fringe obtained through co-propagation of both interfering pulses as recorded for different delays between the two pulses by the CCD camera at the exit of the vacuum chamber (see Figure 5.13). In addition, they depict the significant role of the mirror SM3, which by proper use, eliminates the shifting of the spatial fringes at different delays due to the relative tilt of the pulse fronts. A similar effect has been observed by N. A. Papadogiannis *et al.* [3] for the case I of Ref. [2].

5.5.3 Vacuum Chamber

The beam propagation is occurring in a stainless steel vacuum chamber the purpose of which is to avoid third harmonic generation in the between-image of the TH generation static cell (NLM-1) and the interaction region in the second static cell (NLM-2) as well as to reduce dispersion through propagation. The chamber has an internal diameter of about ~71cm while its volume is of ~99000 cm^3. The vacuum chamber is pumped by an ALCATEL turbo pump having a pumping speed of 400L/s. Typical vacuum pressures used during the experiments are from 8×10^{-5} to 4×10^{-4} mbars.

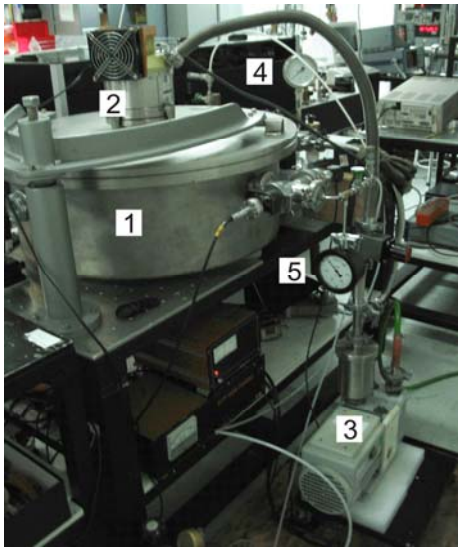

Figure 5.12: The vacuum chamber and the vacuum pumping system used. 1: Vacuum chamber. 2: Alcatel turbo pump. 3: Rotary pump. 4: Pressure gauge for the generation cell. 5: Pressure gauge for the detection cell.

5.5.4 Data Acquisition

Figure 5.13 depicts a schematic diagram of the optical and the data acquisition layout used. The detector is a photodiode sensitive in UV radiation, connected with a digital oscilloscope. The digital oscilloscope is triggered by the 1 kHz repetition rate of the laser. Both, the stepper-motor and the oscilloscope are driven by a computer program. The signal obtained from the oscilloscope as a function of the position of the stepper-motor, is stored in the computer. A CCD camera sensitive in UV radiation is used to image the interaction region in the second static-cell as well as to verify the co-propagation of the beams.

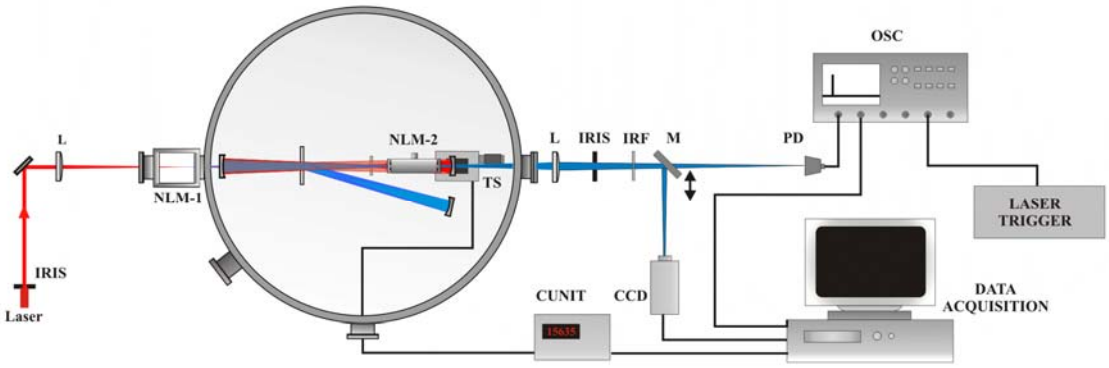

Figure 5.13: Schematic optical and data acquisition layout. A lens L is used to focus the outcoming from the vacuum chamber beams on a Photodiode PD after passing through an IR filter to filter out the fundamental beam. The photodiode is connected with a digital oscilloscope OSC triggered by the 1 kHz repetition rate of the laser. TS is a stepper-motor translation stage. The computer is used to store the signal obtained from the oscilloscope as a function of the stepper-motor's position. A CCD camera (model: COHU 8200) is used to image the co-propagating beams. M is a flat mirror and IRIS is an aperture.

5.5.5 Stepper-Motor calibration

The necessary requirement for an adequate precision scanning device at the wavelength of interest is a reliable translation stage having a resolution in the nanometer range. For this purpose a stepper-motor is used. Usually, such devices are designed to perform measurements with high linearity in micrometer or sub-micrometer scale. Our stepper-motor is a Microcontrole translation stage equipped with a control module that reduces the step-size to few nanometers. This control unit is driven by a Labview program shortening the stepper-motor's default step-size. In the following we use this available option in order to calibrate the device and to test its linearity in this resolution range.

The calibration has been performed by recording the field autocorrelation of the infrared (IR) laser pulse at 800-nm for three different values of the available resolution. The recorded signal is the average of 5 samples per step. Figure 5.14(a) shows an observed modulation of the intensity signal using the default resolution. The resolution, in this case, has been estimated to be ~90-nm (i.e. ~9 points per optical cycle). Note that the resolution of the stepper-motor is the half of this value due to retro-reflection of the beam from the spherical mirror that is mounted on it. This resolution reaches the lowest limit value of 3 points per TH (267nm) optical cycle. Thus, it cannot be used to record an interferometric trace.

On the other hand, Figures 5.14(b) and (c) show the observed signal using two additional available resolution options. In these cases, the resolution is estimated to be ~50-nm (i.e. ~16 points per optical cycle) and ~20-nm (i.e. ~40 points per optical cycle) per TH optical cycle, respectively. Both are providing an adequate resolution with high linearity in order to resolve a modulation at the TH wavelength. In particular, the first case would result ~5 points per TH optical cycle and the latter ~13 points.

Note that the observed structures in Figure 5.14(c) within the optical cycle are a result of the stepper-motor's non-linear behavior to this selected resolution indicating the limits of its working performance. Due to these observations all the following experimental measurements have been carried out by using the resolution used in the recording of Figure 5.14(b).

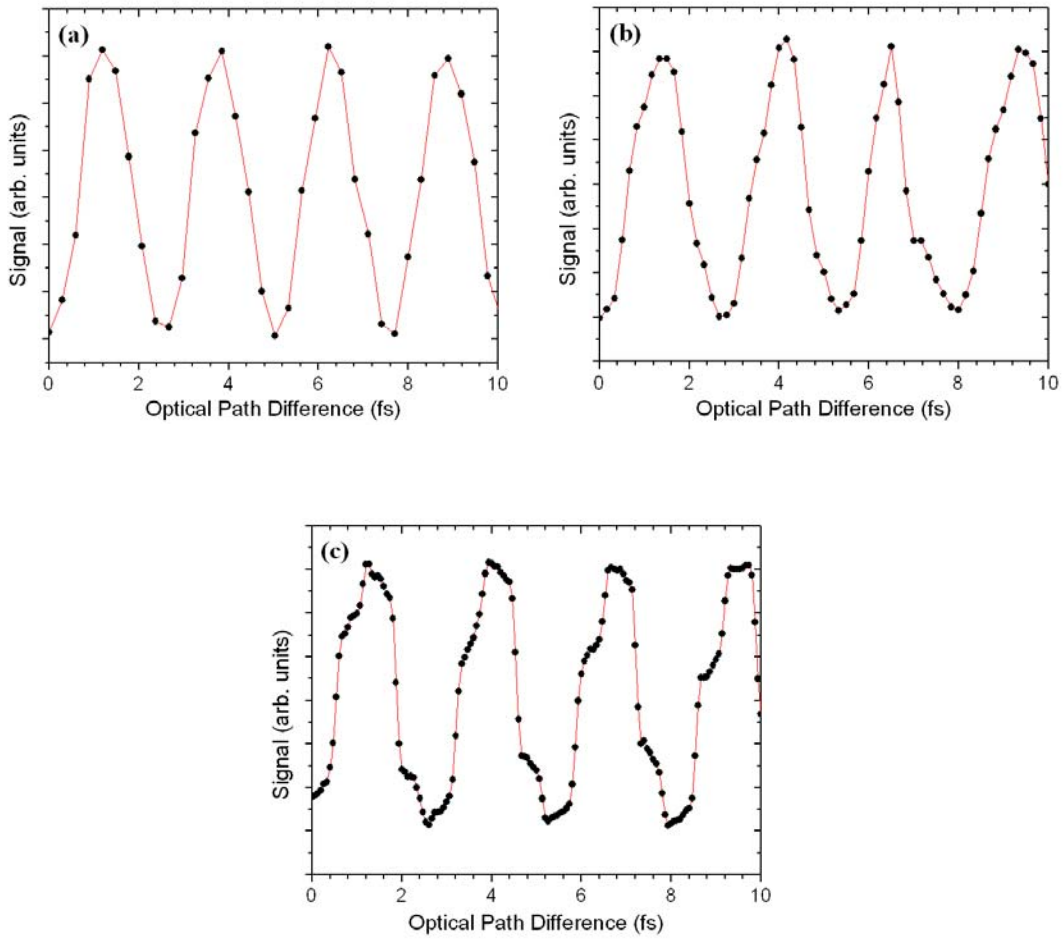

Figure 5.14: Stepper-motor calibration performed through field autocorrelation measurements of the IR laser pulse by using three different translation steps available from the motor's control unit. A ~88-nm (a), ~50-nm (b) and ~20-nm (c) step-size is achieved by scanning across the optical path difference OPD. Figures depict an expended area of the field autocorrelation between 0-10 fs.

5.5.6 Stability of the experimental set-up

In this Section we provide estimations for the experimental stability concerning the interferometric design as well as methods used for the isolation from local noise sources. We also discuss some possible interventions useful for future improvements of the experimental set-up.

Maximization of the temporal resolution requires stable experimental conditions. Noises from any kind of environmental sources have the tendency to affect the stability of interferometric set-ups. Therefore, optimum environmental conditions have to be found and local noise sources to be isolated. In the following different types of local noise sources encountered in our experimental set-up, are discussed. These are mainly due to mechanical vibrations and thermal effects.

Mechanical noise sources originate from vibrations coming from the mechanical parts of the set-up itself, e.g. the translation stage and the vacuum pumping system, as well as vibrations from the surrounding environment. Speaking for vibrations it is worth to give first an estimation of the length scales involved in our experiment. The TH generated from a Ti:Sapphire laser pulse (800-nm) has a wavelength of 266-nm. Measuring an interference effect of such length scales requires at least ~80-nm of overall stability from the optic elements of the set-up, according to the minimal requested resolution mentioned in Section 5.5.5. But this is already below the disturbances caused, for example, from human activities (~5-μm) or even worst, from the mechanical units existing in the surrounding area such as pump laser's power supply units or pump laser's water circulators. In addition, mechanical disturbances are caused by the vacuum pumping system where used to be the main noise source. Figure 5.15(a) depicts a characteristic example of an interferometric measurement performed with IR pulses showing the effect of mechanical noise contributing to the set-up's stability.

In order to overcome such disturbances we performed passive isolation methods. Therefore, thick rubber pads (damping material) are placed under the optical table as well as under all the mechanical noisy units of the surrounding environment. In addition, a damping ring is placed under the turbo pump, although all the optical elements in the vacuum chamber are mounted on thick heavy mounts, providing on this way a fair mechanical isolation. Figure 5.15(b) depicts an interferometric measurement after isolation from mechanical noise sources. The improvement is obvious.

Thermal effects might be also an important factor for the set-up's stability. In fact, an experimental environment with stable temperature conditions is of great importance in performing interferometric measurements. By placing the interferometer into the vacuum chamber offers the possibility to avoid such disturbances. Additionally,

thermal disturbances due to heating of the stepper-motor during the acquisition are avoided by grounding it with a copper wire. This allows the heat to be transferred through the wire to the environment.

Finally, additional noise is induced by intensity fluctuations of the laser system as well as by shot noise of the photodiode current. Intensity fluctuations comprise an important factor for the THG. THG depends on the third power of the fundamental's intensity and thus stable intensity is highly required. Longer averaging reduces the effect of random intensity fluctuations. Intensity fluctuations could also be avoided by installing a photodiode bridge circuit in the laser system [6], in future experiments.

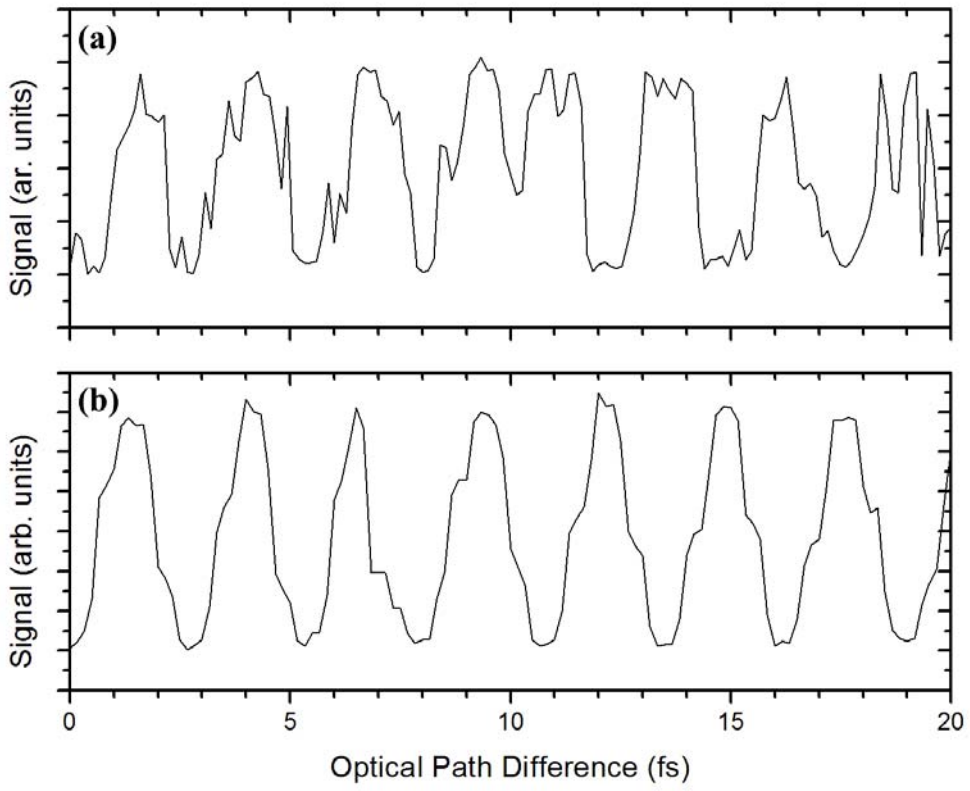

Figure 5.15: Autocorrelation measurements of the IR laser pulse in the case where the interferometer, (a) is not isolated from mechanical noise sources and (b) when is isolated. Apart from the observed noise in the trace, a distortion from the linearity of the Optical Path Difference scan is clearly observed at about 10-fs in Figure (a).

5.6 Results and Discussion

5.6.1 Optimization of the TH signal

Since the harmonic generation is a coherent process, the signal is expected to dependent quadratically on the atomic gas pressure [7,8]. This is a macroscopic effect dealing with the harmonic electric fields generated by each individual atom added coherently to obtain the overall harmonic signal. Figure 5.16 shows the measured dependence of the TH signal generated in the first static-cell as a function of the pressure of Xe-gas. The signal tends to reach a maximum value at around 100-mbars of pressure. The intensity of the focused beam into the NLM-1 is of ~2×10^{14} W/cm^2.

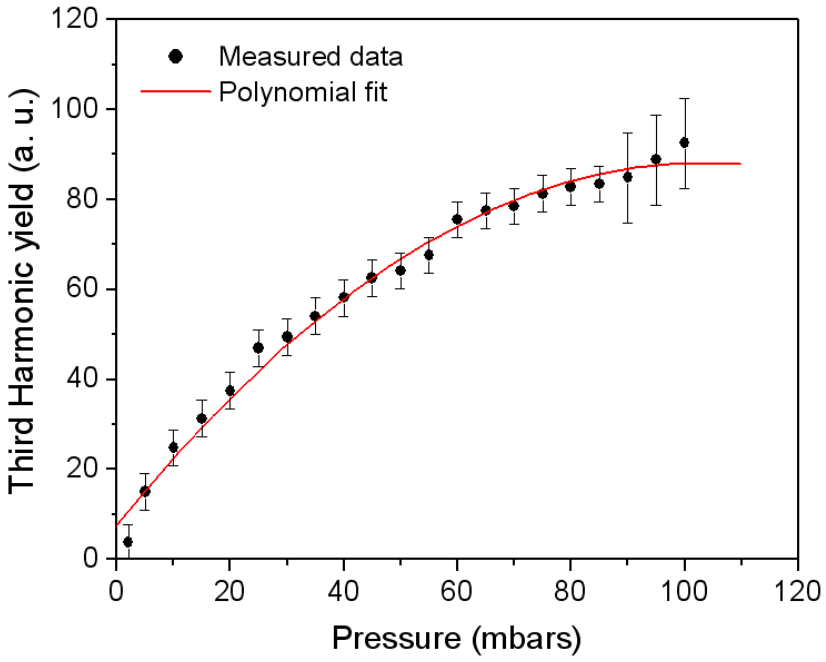

Figure 5.16: The dependence of the third harmonic signal generated into the first gas-cell on the pressure of the used Xe gas. The red line depicts the fit curve to the measured points showing the nearly maximum efficiency of the generated third harmonic at around 100-mbars and the dependence of the TH on the gas pressure.

5.6.2 Intensity-dependence measurements

In order to verify the order of non-linearity contributing to the signal of the third harmonic generated in the first gas-cell, we measured the dependence of this signal as a function of the intensity of the fundamental pulse. The TH signal follows the LOPT power-law I^N. The energy of the ~56-fs fundamental pulse was changed in the interval 60-450μJ, by using a variable 1-mm-thick neutral density filter. Hence the pulse duration is kept close to its Fourier-transform limited value. These values correspond to a pulse intensity ranging from 3.5×10^{13} to 2×10^{14} W/cm^2 (see Appendix B). The Xe-gas pressure is adjusted to 80-mbars close to the value reflecting the maximum efficiency, as found in the preceding Section. Figure 5.17 shows the energy dependence in logarithmic scale. The red line depicts the fit function to the measured data showing the non-linearity of the measured signal. The measured slope is found to be N = 2.5 ± 0.2 which is a value very close to that expected from the third power-law for this intensity interval used.

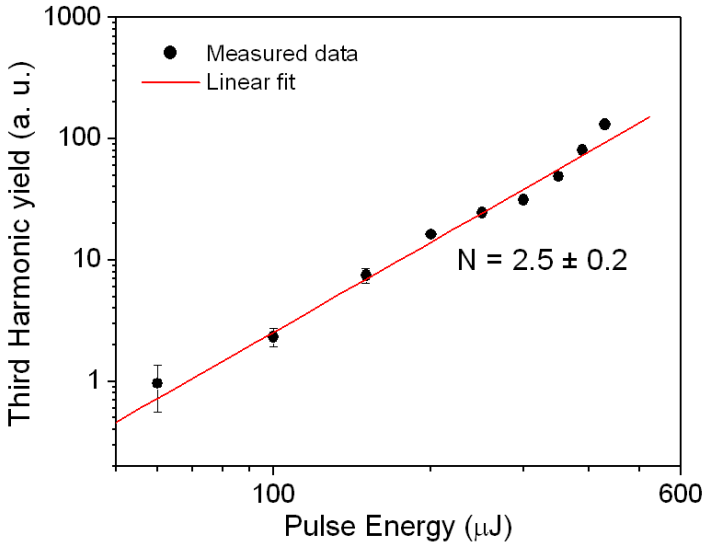

Figure 5.17: Energy dependence of the third harmonic yield at the first gas-cell. Filled cycles show the measured data as a function of the fundamental pulse energy. The graph is depicted in logarithmic scale. The red line depicts the fit function to the measured data showing the non-linearity of the measured signal.

The total intensity used in these experiments could generate even high-order harmonics, but their contribution to the measured signal is precluded from the optics used (e.g. fused silica grating and windows) and the geometry of the interferometer itself.

5.6.3 Cross-correlation measurements

The fundamental pulse having an energy of 360 μJ and a FWHM duration of 70 ± 8-fs is focused into the first gas-cell filled with 70-mbars of Xe. The fundamental has been negatively chirped to maximize the TH signal generated in the first gas-cell. This has been done in order to compensate the chirp that is introduced to the fundamental as it passes through the optics before being focused into the NLM-1. The profile of the chirped fundamental pulse has been determined by measuring the amount of chirped introduced from the optics separately. Traces of both the spectral and temporal profile of the fundamental pulse measured with the SPIDER are depicted in Figure 5.18. The first-first-order of the diffracted TH pulse and the zeroth-zeroth-order diffracted fundamental are focused into the second static-cell filled with 4-mbars of Xe-gas. The pressure of the gas in the NLM-2 is adjusted to this value in order to maximize the visibility of the spatial interference signal between the two generated TH pulses (i.e. the one generated into the NLM-2 and that generated into the NLM-1).

Figure 5.19(a) shows the measured in the second cell cross-correlation trace obtained by scanning the fundamental across the generated in the first static-cell TH pulse. The average value of 10 samples per step, is recorded. The inset in (a) depicts an expanded area of the cross-correlation trace between 0-10 fs showing the modulation of the signal in more detail. For better visibility of the cross-correlation envelope, Figure 5.19(b) depicts the time-derivative of (a). By this, the low-frequency components are suppressed and the high-frequency components of interest are enhanced. Thus, for a modulated signal, $A(t) = \cos(\omega_{low}t) + \cos(\omega_{high}t)$, consisting of a low-frequency ω_{low} and a high-frequency ω_{high}, with $\omega_{low} << \omega_{high}$, the derivation gives

$$\frac{dA(t)}{dt} = -\left(\omega_{low}\sin(\omega_{low}t) + \omega_{high}\sin(\omega_{high}t)\right) \approx -\omega_{high}\sin(\omega_{high}t)\,. \qquad (5.2)$$

The red line in Figure 5.19(b) depicts the fit Gaussian envelope of the interferometric trace. This gives the coherence length of the two correlated pulses that is of ~35-fs.

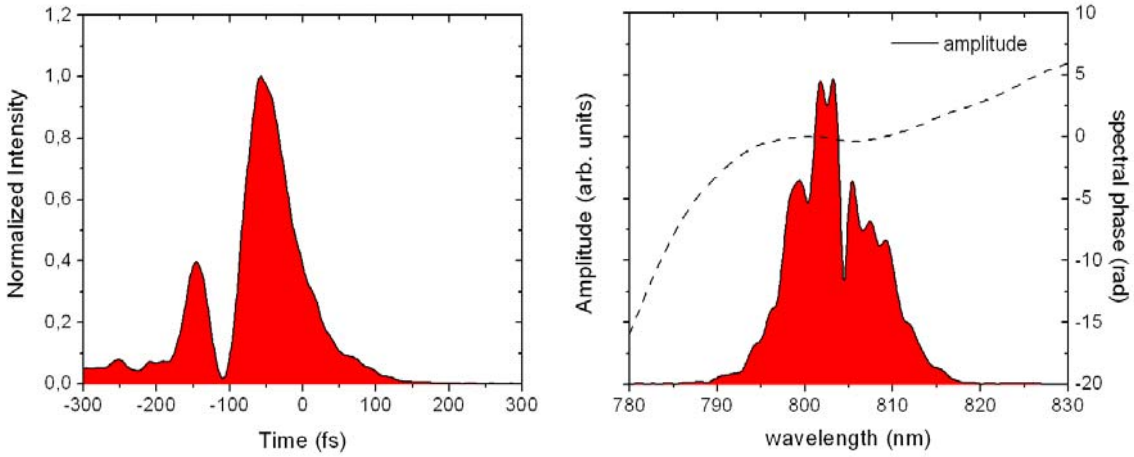

Figure 5.18: *Left:* The temporal and *Right:* the spectral profile of negatively chirped fundamental pulse measured with the SPIDER apparatus. The dashed curve in the right figure represents the measured spectral phase distribution.

The maximum observed modulation depth, defined as

$$M = \frac{I_{\max} - I_{\min}}{2(I_{\max} + I_{\min})}, \tag{5.3}$$

where I_{max} is the maximum and I_{min} is the minimum of the modulated signal (e.g. ion signal intensity), of the interferometric trace in Fig. 5.19(a) is found to be ~0.06, showing an adequate contrast to resolve the trace.

Figure 5.19(c) depicts the Fourier-transform spectrum of the cross-correlation trace in (a). This shows the spectral profile as a product of the interaction between the corresponding interfering channels into the detection cell (NLM-2). The cross-correlation trace, in this particular case, oscillates at the TH frequency (~1.13 1/fs). To retrieve the spectral phase we used the expression $\varphi(\omega) = \mathrm{Im}(\ln A(\omega))$, where $A(\omega)$ is the extracted spectral amplitude from the Fourier-transform (see Appendix C). The dash-dot line shows the retrieved spectral phase across the third harmonic peak. Note

that all the spectra recorded under these conditions showed a reproducible spectral phase distribution across the harmonic peak. The chirp value is found by fitting a linear function on the data points (red line) and is equal to (205 ± 5) rad•fs.

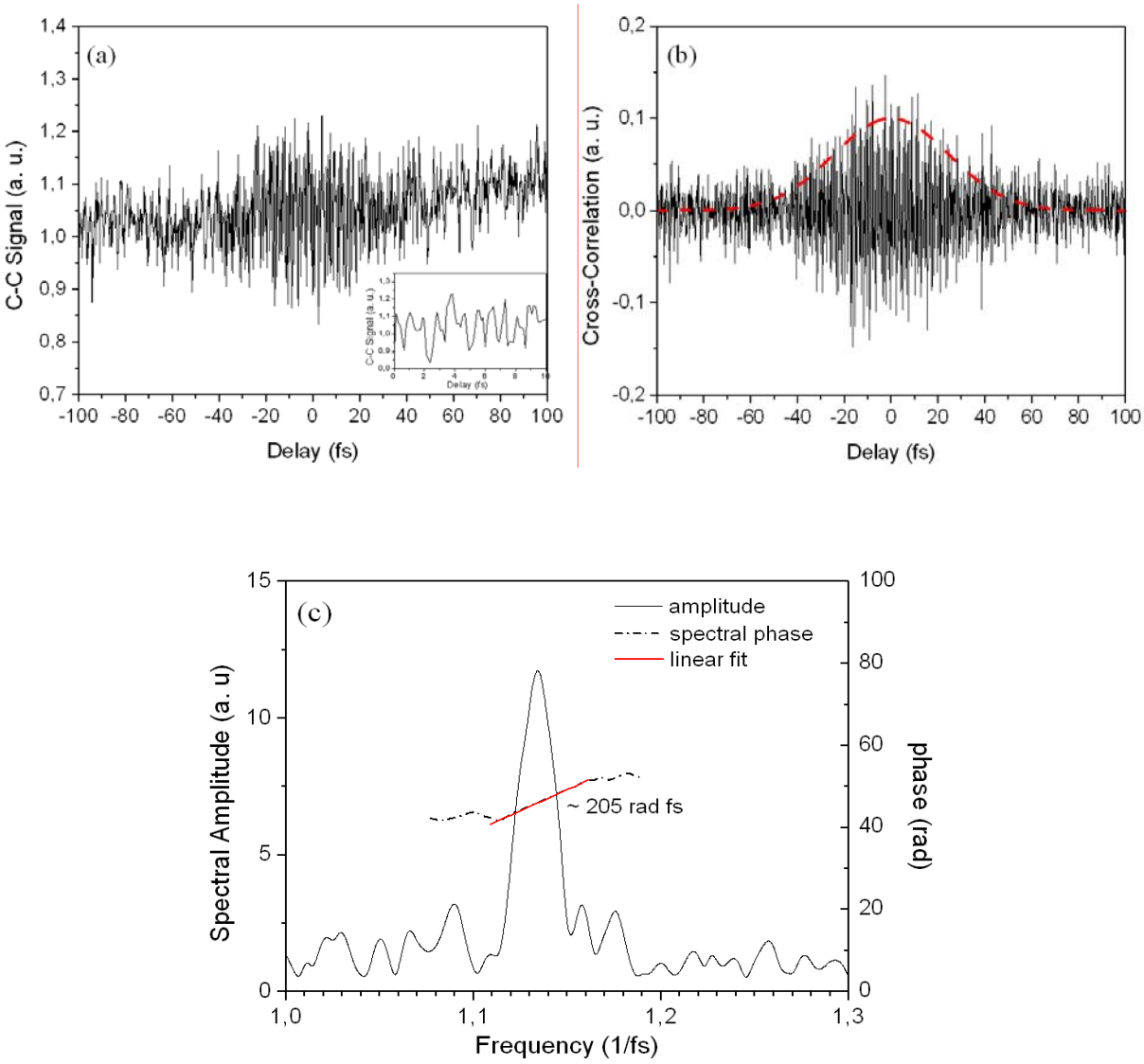

Figure 5.19: (a) Cross-correlation trace obtained by scanning the fundamental pulse across the TH pulse that is generated into NLM-1. (b) The time-derivative of the trace (a). The red line depicts the fit Gaussian envelope to the cross-correlation trace (c) Fourier-transform spectrum of the cross-correlation trace in (a). The dash-dot line depicts the retrieved spectral phase across the spectrum.

To retrieve the spectral amplitude of the TH pulse (i.e. that generated in the NLM-1) a field autocorrelation measurement, is performed. For this purpose spatial interference of the recombined diffracted zeroth-first-order and the diffracted first-zeroth-order of the TH pulse, by properly positioning the mirror SM3, is recorded. THG conditions were the same as in the case of the cross-correlation. Figures 5.20(a) and (b) show the measured first-order AC signal and its time-derivative, respectively. The inset in (a) depicts the modulation in detail. The red line in (b) shows a Gaussian envelope fit to the autocorrelation trace, having a FWHM of ~35-fs and showing the coherence time of the TH field. Figure 5.20(c) shows the Fourier-transform spectrum of the trace (a).

Figure 5.21 depicts the reconstructed TH obtained by Fourier-synthesis

$$F(t) = \sum_{j=1}^{N} \sqrt{S(\omega_j)} \exp(i\phi(\omega_j)) \exp(i\omega_j t), \tag{5.4}$$

using the above retrieved spectral amplitude $\sqrt{S(\omega_j)}$ and spectral phase distribution $\phi(\omega_j)$. In eq.(5.4) N is the number of the sampling points. The pulse duration found by fitting a Gaussian function on the reconstructed pulse is 31 ± 2fs. The mean value found by a series of measurements is 32 ± 5fs. The resulted duration in combination with the measured duration of the fundamental pulse is, within the experimental error, in good agreement with that expected from the lowest-order perturbation theory i.e. ~33-fs as obtained from eq. (4.11). Note that similar values have been measured by Papadogiannis *et al.* through second-order AC [3].

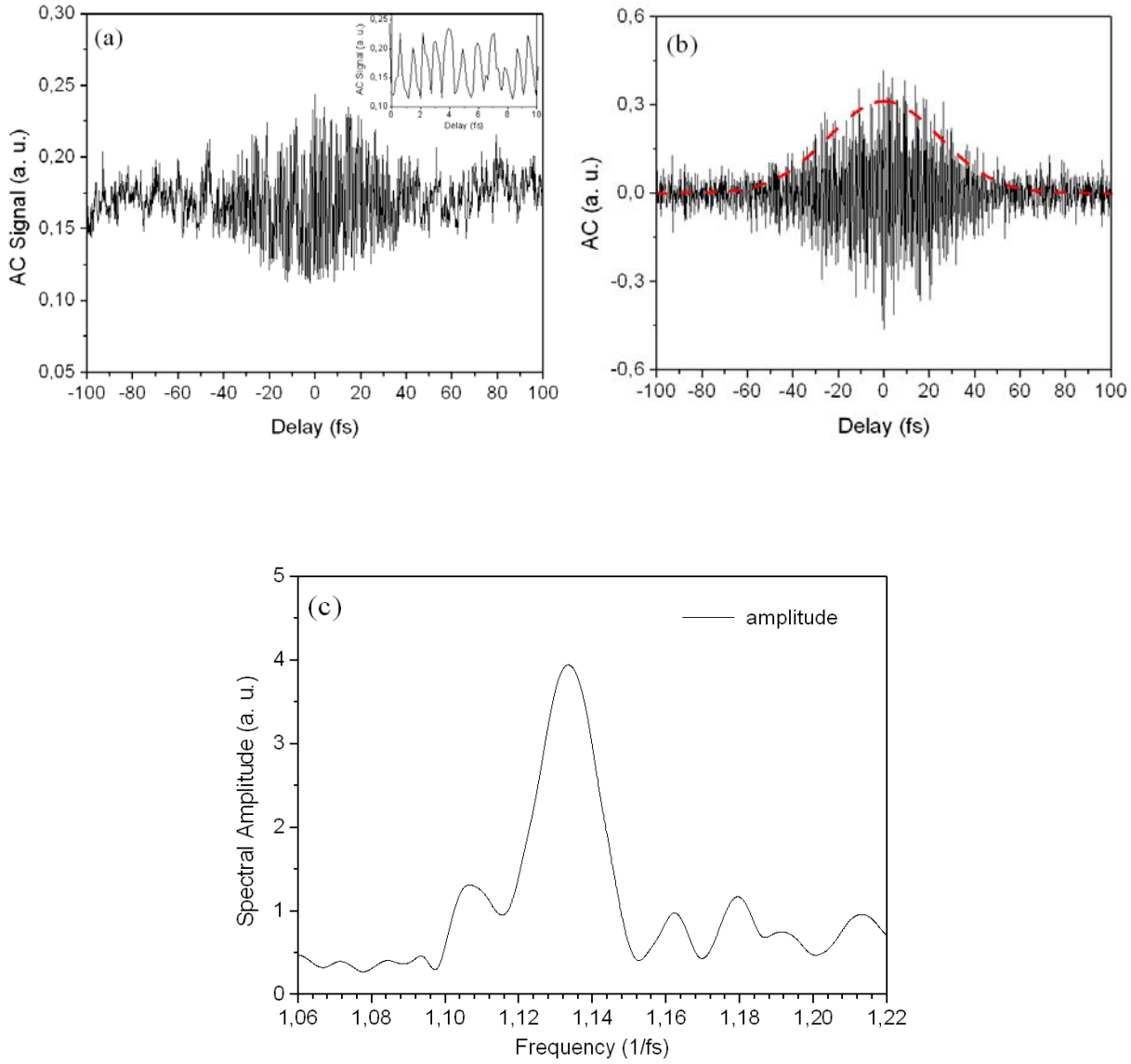

Figure 5.20: (a) First-order autocorrelation trace of the TH field. The inset depicts an expanded area between 0-10 fs showing the modulation in detail. (b) The time-derivative of the trace (a). (c) The Fourier-transform spectrum of the trace of (a).

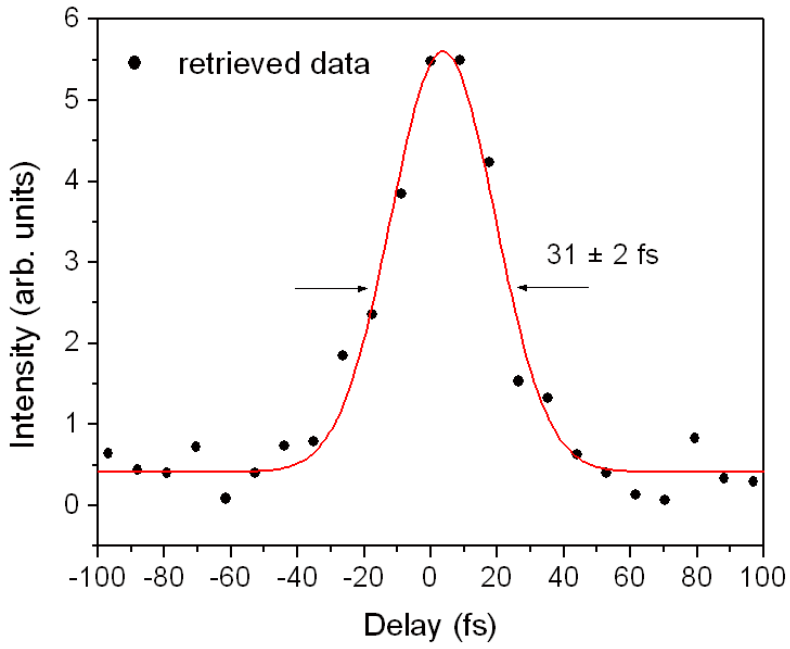

Figure 5.21: The reconstructed is through Fourier-synthesis using the retrieved spectral phase distribution of the cross-correlation data of Fig. 5.19 and the spectral amplitude distribution of Fig. 5.20. The duration found by fitting a Gaussian function is 31 ± 2 fs.

5.7 Conclusion and Future Aspects

In conclusion, we have performed cross-correlation measurements between the fundamental field of a Ti:Sapphire laser system and its third harmonic in order to characterize the TH pulse. Characterization is through the "phase-control" technique described in Ref. [1]. The generation has been optimized by adjusting the pressure of the generation gas. For the optimized TH signal the spectral amplitude distribution has been determined through first-order AC measurements. The spectral phase distribution has been retrieved through the cross-correlation measurements. The TH pulse is reconstructed through Fourier-synthesis of the above. Moreover, a TH pulse duration of 32 ± 5fs has been found that is in good agreement with that expected from the lowest-order perturbation theory i.e. ~33-fs, confirming thus the dispersionless operation of the experimental set-up.

It is worth noting that the implementation of this technique has been performed by using, for the first time, the transmission grating interferometer in the geometry of the case III in Ref. [2]. A detailed investigation on the performance and the stability of the interferometer has been presented showing its limitations and ways of improvement.

The measured value of the TH pulse duration is practically a Fourier-transform limited value. As immediate future work, additional experiments could be performed in order to characterize chirped TH pulses by introducing GVD into the generated TH pulse in NLM-1. This complementary study would demonstrate in a more complete manner the advantage of the present technique from other cross-correlation approaches.

Finally, the present work opens up interesting perspectives for the characterization of ultra-short pulses, which in the future can be extended to shorter wavelengths and in the attosecond time-scale.

Appendices

Appendix A. Perturbation Theory and Multi-photon absorption

In the following we will give same useful expressions of the multi-photon absorption of an atom interacting with a laser field. Analytical solutions can be found in Refs. [1,2]. We assume an atomic wavefunction $|\psi(r,t)\rangle$ that obeys the time-dependent Schrödinger equation

$$i\hbar \frac{\partial}{\partial t}|\psi(r,t)\rangle = \hat{H}|\psi(r,t)\rangle, \tag{A.1}$$

where the Hamiltonian $\hat{H}$ is given as: $\hat{H} = \hat{H}_{atom} + V(t)$. $\hat{H}_{atom}$ is the Hamiltonian of a free atom, while $V(t)$ is the interaction potential energy with the applied optical field given by

$$V(t) = -\vec{\mu}\tilde{E}(t). \tag{A.2}$$

Here $\vec{\mu} = -e\vec{r}$ is the electric dipole moment and E(t) is the applied time-dependent electric field. For simplicity we can assume a monochromatic linearly polarized electric field of the form

$$\tilde{E}(t) = E_0 \exp[-i\omega t] + c.c, \tag{A.3}$$

where *c.c.* denotes the complex conjugate. Since the eigenstates of the atom form a complete set we can express the solution of eq. (A.1) as the linear combination of these eigenstates. Thus

$$|\psi(r,t)\rangle = \sum_n a_n(t)|u_n(r)\rangle \exp(-i\omega_n t), \tag{A.4}$$

where $u_n(r)\exp(-i\omega_n t)$ are the known eigenstates of the atom. By substitution of eq. (A.4) to the eq. (A.1) we can solve the Schrödinger equation as a function of the time-dependent coefficients α_n, thus to obtain

$$i\hbar\sum_n \frac{da_n(t)}{dt}\left|u_n(r)\right\rangle \exp[-i\omega_n t] + \hbar\omega_n \sum_n a_n(t)\left|u_n(r)\right\rangle \exp[-i\omega_n t] =$$

$$\sum_n a_n(t)E_n\left|u_n(r)\right\rangle \exp[-i\omega_n t] + \sum_n a_n(t)V\left|u_n(r)\right\rangle \exp[-i\omega_n t], \qquad \text{(A.5)}$$

where $E_n = \hbar\omega_n$ are the eigenenergies. To simplify the last equation we can use the orthogonality of the eigenstates of the atom by multiplying with their orthogonal complex conjugates and by integrating over all space. Thus we obtain the matrix form solution

$$i\hbar\frac{da_m(t)}{dt} = \sum_n a_n(t)V_{mn}\exp[-i\omega_{nm}t], \qquad \text{(A.6)}$$

where $\omega_{nm} = \omega_n - \omega_m$ and $V_{nm} = \left\langle u_m(r)\right|V\left|u_n(r)\right\rangle$ is the matrix element of the interaction Hamiltonian. The general eq. (A.6) cannot be solved exactly. Thus it must be solved using perturbation expressions by which we expand α_m in powers of the interaction as $\alpha_m(t) = \alpha_m^{(0)}(t) + \alpha_m^{(1)}(t) + \alpha_m^{(2)}(t) + \ldots$ Thus, the N-th power expression of the eq. (A.6), under this assumptions, is given by

$$\frac{da_m^{(N)}(t)}{dt} = (i\hbar)^{-1}\sum_n a_n^{(N-1)}V_{mn}\exp[-i\omega_{nm}t]. \qquad \text{(A.7)}$$

The Linear Absorption

We can now see an example of how the latter equation can be solved. We assume the simplest case of the linear absorption. We set $N = 1$ which corresponds to the first-order interaction of the atom with the field. We assume further that the atom is initially in its ground state $\left|g\right\rangle$ before the field is applied to excite the atom to the final state $\left|f\right\rangle$. Thus, $\alpha_g^{(0)} = 1$ and $\alpha_n^{(0)} = 0$. Equation (A.7) then becomes

$$\frac{da_f^{(1)}(t)}{dt} = -(i\hbar)^{-1}\mu_{fg}\left[E_0\exp[-i(\omega_{fg}-\omega)t] + E_0^*\exp[-i(\omega_{fg}+\omega)t]\right]. \quad \text{(A.8)}$$

The eq. (A.8) can be integrated in time to give the expression for the time-dependent first-order probability amplitude $\alpha^{(1)}(t)$.

$$a_f^{(1)}(t) = \frac{\mu_{fg}E_0}{\hbar(\omega_{fg}-\omega)}\left[\exp[-i(\omega_{fg}-\omega)t'] - 1\right] + \frac{\mu_{fg}E_0^*}{\hbar(\omega_{fg}+\omega)}\left[\exp[-i(\omega_{fg}+\omega)t'] - 1\right] \quad \text{(A.9)}$$

The second term of the above equation can be eliminated by using the rotating wave approximation. Therefore, the transition probability is given as

$$W_{fg} = \left|a_f^{(1)}\right|^2 = \left|\frac{\mu_{fg}E_0}{\hbar}\right|^2 \left|\frac{\left[\exp[-i(\omega_{fg}-\omega)t'] - 1\right]}{(\omega_{fg}-\omega)}\right|^2 . \quad \text{(A.10)}$$

Making now use the Fermi's golden rule, the excitation rate is given by

$$R_{fg} = \frac{W_{fg}}{t} = 2\pi\left|\frac{\mu_{fg}E_0}{\hbar}\right|^2 \rho(\omega_{fg}=\omega), \quad \text{(A.11)}$$

where ρ is the Lorentzian line-shape function where the density of the final state(s) is to be evaluated at frequency ω of the incident field. The linear absorption is often described as a function of the linear absorption cross-section $\sigma^{(1)}$ defined such that

$$R_{fg} = \sigma_{fg}^{(1)} I , \quad \text{(A.12)}$$

where I is the intensity of the incident light and

$$\sigma_{fg}^{(1)} = \frac{4\pi^2}{nc}\left|\frac{\mu_{fg}}{\hbar}\right|^2 \rho(\omega_{fg}=\omega), \quad \text{(A.13)}$$

where n is the refractive index of the medium and c is the speed of light in vacuum.

The Multi-photon Absorption

By following the same concept we can extract the transition probabilities and rates for a multi-photon process. Next we give the expressions of the transition rates for the third and *N*-th order result from a third and *N*-th order non-linear absorption process, respectively.

$$R_{fg} = 2\pi \sum_{nm} \left| \frac{\mu_{fn}\mu_{nm}\mu_{mg}E_0^3}{\hbar^3(\omega_{ng} - 2\omega)(\omega_{mg} - \omega)} \right|^2 \rho(\omega_{fg} - 3\omega) \tag{A.14}$$

$$R_{fg} = 2\pi \sum_{nms\ldots} \left| \frac{\mu_{fn}\mu_{nm}\mu_{ms}\ldots\mu_{qg}E_0^N}{\hbar^N(\omega_{ng} - N\omega + \omega)\ldots(\omega_{ng} - 2\omega)(\omega_{mg} - \omega)} \right|^2 \rho(\omega_{fg} - N\omega) \tag{A.15}$$

Appendix B. Relationship between Intensity and Field-strength

The associated intensity, of the electric field *E,* in cgs units, is given by:

$$I = \frac{nc}{2\pi}\left|\vec{E}\right|^2, \tag{B.1}$$

where n is the refractive index and c is the speed of light in vacuum equal to 3×10^{10} cm/s^2. I is measured in erg/cm^{2}s. In SI units the intensity is given by

$$I = \frac{2n}{Z_0}\left|\vec{E}\right|^2, \tag{B.2}$$

where $Z_0 = 377\ \Omega$ is the impendence. I is measured in W/m^2. Given the average power $\overline{P}$ of a pulsed laser having a repetition rate T, the energy of the pulse will be $Q = P/T$. If the beam is focused to a spot-size of w_0, then the pulse intensity will be

$$I = P/\pi w_0^2 = Q/t_p\pi w_0^2, \tag{B.3}$$

where t_p is the pulse duration.

Appendix C. Mathematica code used to extract the spectral phase

The following code is used to extract the spectral phase from the cross-correlation measured data. After having performed FFT on the data, the code imports the real α and imaginary β frequency dependent values of the spectral amplitude components contained in the file, e.g. "File.dat".

Assuming a complex spectral amplitude $A(\omega) = \alpha(\omega) + i\beta(\omega) = A_0(\omega)e^{i\varphi(\omega)}$, where $A_0(\omega) = \sqrt{\alpha^2(\omega) + \beta^2(\omega)}$ and the spectral phase is given by

$$\varphi(\omega) = \arctan\left[\frac{\mathrm{Im}[A(\omega)]}{\mathrm{Re}[A(\omega)]}\right] = \mathrm{Im}[\ln(A(\omega))], \qquad \text{(C.1)}$$

The retrieved phase distribution is located within the interval $-\pi/2 < \varphi < \pi/2$. The code unwraps the phase in order to get the correct phase across the spectrum.

The Mathematica code:

```
<< LinearAlgebra`MatrixManipulation`
field = Import["File.dat", "Table", ConversionOptions → {"NumberPoint" → ","}];

shift = 0;
n = 0;
xdim = Dimensions[field][[1]];
phase = Table[0, {xdim}];
Do[
 phase[[i]] = Im[Log[field[[i, 1]] + I * field[[i, 2]]]] + shift;
 If[phase[[i]] - phase[[i - 1]] ≤ -Pi / 2,
  n = n + 1;
  shift = n * Pi;
  phase[[i]] = phase[[i]] + Pi;];
 If[phase[[i]] - phase[[i - 1]] ≥ Pi / 2,
  n = n - 1;
  shift = n * Pi;
  phase[[i]] = phase[[i]] - Pi;];
 , {i, 2, Dimensions[field][[1]]}]

ListPlot[phase, PlotJoined → True, PlotRange → {All, All}];
Export["Filenew.dat", phase, "Table"];
```

References

Chapter 1:

[1]. F. Krausz, *Physics World*, (Sept. 2001)

[2]. G. Steinmeyer *et al.*, *Science*, **286**, 150, (1999)

[3]. T. W. Hänsch, *Opt. Commun.*, **80**, 70, (1990).

[4]. A. E. Kaplan, *Phys. Rev. Let.*, **73**, 1243, (1994).

[5]. S. E. Harris *et al.*, *Phys. Rev. Let.*, **81**, 2984, (1998).

[6]. Gy. Farkas and Cs. Tóth, *Phys. Lett. A*, **168**, 447, (1992).

Chapter 2:

[1]. L. D. Landau, and E. M. Lifshitz, *Quantum Mechanics*, Pergamon-Oxford, (1977).

[2]. R. Loudon, *The Quantum theory of Light*, 2nd Edition - Oxford Science, Oxford, (1991).

[3]. L. E. Lompré *et al.*, *J. Opt. Soc. Am.*, **7**, 527, (1985).

[4]. R. Wagner, S.-Y. *et al.*, *Phys. Rev. Lett.*, **78**, 3125, (1997).

[5]. P. Monot, *et al.*, *Phys. Rev. Lett.*, **74**, 2953, (1995).

[6]. M. Protopapas, C. H. Keitel, and P. L. Knight, *Rep. Prog. Phys.*, **60**, 389, (1997).

[7]. L. V. Keldysh, *Sov. Phys, JETP*, **20**, 1307, (1965).

[8]. P. B. Corkum, *Phys. Rev. Lett.*, **71**, 1994, (1993).

[9]. K. J. Schafer *et al.*, *Phys. Rev. Lett.*, **70**, 1599, (1993).

[10]. Anne L'Huillier, and Ph. Balcou, *Phys. Rev. Lett.*, **70**, 774, (1993).

[11]. J. J. Macklin *et al.*, *Phys. Rev. Lett.*, **70**, 766, (1993).

[12]. M. Lewenstein *et al.*, *Phys. Rev. A*, **49**, 2117, (1994).

[13]. T. Ditmire *et al.*, *Phys. Rev. Lett.,* **77**, 4756, (1996).

[14]. L. Le Déroff *et al.*, *Phys. Rev. A*, **61**, 043802, (2000).

[15]. M. Bellini *et al.*, *Phys. Rev. Lett.*, **81**, 297, (1998).

[16]. P. Salières *et al.*, *J. Phys. B: At. Mol. Opt. Phys.*, **27**, L217, (1994).

[17]. J. W. G. Tisch. *et al.*, *Phys. Rev. Lett.*, **80**, 1204, (1998).

Chapter 3:

[1]. J.-C. M. Diels and W. Rudolf, *Ultrashort Laser Pulse Phenomena*, (Academic Press, 1996).

[2]. J.-C. M. Diels *et al.*, *Appl. Opt.*, **24**, 1270, (1985).

[3]. E. P Ippen and C.V. Shank, *Ultrashort Light Pulses – Picosecond Techniques and Applications,* (Spinger – Verlag, Berlin, 1977).

[4]. J. A. Giordmaine *et al.*, *Appl. Phys. Lett.*, **11**, 216, (1985).

[5]. N. G. Basov *et al.*, *Sov. J. Quant. Electron.*, **15**, 1429, (1985).

[6]. R. Trebino *et al.*, *Opt. Lett.*, **15**, 1079, (1990).

[7]. J. T. Manassah, *Appl. Opt.*, **26**, 2941, (1987).

[8]. J. Jansky and G. Corradi, *Opt. Commun.*, **60**, 251, (1986).

[9]. N. G. Paulter and A. K. Majumdar, *Opt. Commun.*, **81**, 95, (1991).

[10]. A. S. L. Comes *et al.*, *J. Opt. Soc. Amer. B*, **5**, 373, (1988).

[11]. G. Szabo *et al.*, *Opt. Commun.*, **82**, 56, (1991).

[12]. R. L. Fork *et al.*, *Opt. Lett.*, **8**, 1, (1983).

[13]. J. R. Rothenberg and D. Grischkowsky, *Opt. Lett.*, **12**, 99, (1987).

[14]. R. L Fork *et al.*, *Opt. Lett.*, **12**, 483, (1987).

[15]. J. L. A. Chilla and O. E. Martinez, *Opt. Lett.*, **16**, 39, (1991).

[16]. J. L. A. Chilla and O. E. Martinez, *Opt. Commun.*, **89**, 434, (1992).

[17]. J. L. A. Chilla and O. E. Martinez, *IEEE J. Quant. Electron.*, **27**, 1228, (1991).

[18]. W. Koenig *et al.*, *J. Acoust. Soc. Amer.*, **18**, 19, (1946).

[19]. K. C. Chu *et al.*, *Opt. Lett.*, **20**, 904, (1995).

[20]. J. K. Rhee *et al.*, *J. Opt. Soc. Amer. B*, **13**, 1780, (1996)

[21]. R. Trebino and D. J Kane, *J. Opt. Soc. Amer. A*, **10**, 1101, (1993).

[22]. D. J Kane and R. Trebino, *Opt. Lett.*, **18**, 823, (1993).

[23]. D. J Kane and R. Trebino, *IEEE J. Quant. Electron.*, **29**, 571, (1993).

[24]. D. N. Fittinghoff *et al.*, *J. Opt. Soc. Amer. B*, **12**, 1955, (1995).

[25]. R. Trebino *et al.*, *Rev. Sci. Intrum.*, **68**, 3277, (1997).

[26]. E. B. Treacy, *J. Appl. Phys.*, **42**, 3848, (1971).

[27]. K. W. DeLong *et al.*, *J. Opt. Soc. Amer. B*, **11**, 1595, (1994).

[28]. D. J. Kane *et al.*, *Opt. Lett.*, **19**, 1061, (1994).

[29]. T. Tsang *et al.*, *Opt. Lett.*, **21**, 1381, (1996).

[30]. T. S. Clement *et al.*, *Opt. Lett.*, **20**, 70, (1995).

[31]. J. Sweetser *et al.*, *Opt. Lett.*, **22**, 519, (1997).

[32]. K. W. DeLong *et al.*, *Opt. Lett.*, **20**, 486, (1995).

[33]. A. Baltuska *et al.*, *IEEE J. Quant. Electron.*, **35**, 459, (1999).

[34]. C. Iaconis, and I. A. Wamsley, *Opt. Lett.*, **23**, 729, (1998).

[35]. C. Iaconis, and I. A. Wamsley, *IEEE J. Quant. Electron.*, **35**, 51, (1999).

[36]. C. Froehly *et al*., *J. Opt. (Paris)*, **4**, 183, (1973).

[37]. R. W. Boyd, *Nonlinear Optics,* (Academic press, Second Edition, 2003)

[38]. T. M. Shuman *et al.*, *Opt. Express*, **5**, 134, 1999

[39]. L. Li *et al.*, *Jpn. Soc. Appl. Phys.*, **40**, L684 (2001).

[40]. R. Morita *et al.*, *Meas. Sci. Technol.*, **13**, 1710 (2002).

[41]. M. Hirasawa *et al.*, *Appl. Phys. B,* **74**, S225, (2002).

[42]. N. A Papadogiannis *et al.*, *Phys. Rev. Let.*, **83**, 4289, (1999).

[43]. P. B. Corkum, *Nature*, **403**, 845, (2000).

[44]. N. A. Papadogiannis, and D. Charalambidis, *Phys. Rev. Lett.*, **87**, 109402, (2001).

[45]. G. Tempea *et al.*, *Phys. Rev. Lett.*, **87**, 109401, (2001).

[46]. N. A. Papadogiannis *et al.*, *Opt. Lett.*, **27**, 1561, (2002).

[47]. D. Xenakis *et al.*, *J. Phys. B: At. Mol. Opt. Phys.*, **29**, L457, (1996).

[48]. Y. Kobayashi *et al.*, *Opt. Lett.*, **23**, 64, (1998).

[49]. T. Sekikawa *et al.*, *Phys. Rev. Lett.*, **83**, 2564, (1999).

[50]. D. Descamps *et al.*, *Phys. Rev. A*, **64**, 031404(R), (2001).

[51]. P. Tzallas *et al.*, *Nature*, **426**, 267, (2003).

[52]. T. E. Glover *et al. Phys. Rev Lett.,* **76**, 2468, (1996).

[53]. R. Trebino *et al.*, *Rev. Sci. Instrum.*, **68**, 3277, (1997)

[54]. T. Sekikawa *et al.*, *Phys. Rev. Lett.*, **88**, 193902, (2002).

[55]. J. Norin *et al*. *Phys. Rev. Lett.*, **88**, 193901, (2002).

[56]. J. Mauritsson *et al.*, Phys. Rev. A, 70, 021801(R), (2004).

[57]. H. G. Muller, *Appl. Phys. B*, **74**, S17, (2002).

[58]. J. Mauritsson *et al.*, *Opt. Lett.*, **28**, 2393, (2003).

[59]. V. Véniard *et al., Phys. Rev. A*, **54**, 721, (1996)

[60]. P. M. Paul *et al.*, *Science*, **292**, 1689, (2001).

[61]. S. Kazamias and Ph. Balcou, *Phys. Rev. A*, **69**, 063416 (2004).

[62]. L. Nikolopoulos *et al.*, Phys. Rev. Lett. (Accepted to appear in March 2005).

Chapter 4:

[1]. E. Constant *et al.*, *Phys. Rev. A*, **56**, 3870, (1997).

[2]. A. Scrinzi *et al.*, *Phys. Rev. Lett.*, **86**, 412, (2001).

[3]. M. Drescher *et al.*, *Science*, **291**, 1923, (2001).

[4]. P. M. Paul *et al.*, *Science*, **292**, 1689, (2001).

[5]. E. Hertz *et al. Phys. Rev. A*, **64**, 051801 (2001)

[6]. Ce Chen *et al.*, *Phys. Rev. Lett.*, **64**, 507, (1990).

[7]. Ce Chen *et al.*, *Phys. Rev. Lett.*, **65**, 1737, (1990).

[8]. M. Shapiro *et al.*, *Chem. Phys. Lett.*, **149**, 451, (1988).

[9]. T. Nakajima, and P. Lambropoulos, *Phys. Rev. Lett*., **70**, 1081, (1993).

[10]. N. Takashi, and P. Lambropoulos, *Phys. Rev. A*, **50**, 595, (1994).

[11]. B. Sheehy *et al.*, *Phys. Rev. Lett.*, **74**, 4799, (1995).

[12]. E. Charron *et al.*, *Phys. Rev. Lett.*,**71**, 692, (1993).

[13]. E. Cormier, and P. Lambropoulos, *J. Phys. B: At. Mol. Opt. Phys.*, **30**, 3095, (1997).

[14]. N. E. Karapanagioti *et al.*, *J. Phys. B: At. Mol. Opt. Phys.*, **29**, 3599, (1996).

[15]. D. Xenakis *et al.*, *Opt. Comm.*, **152**, 3599, (1996).

[16]. R. Boyd, *Nonlinear Optics*, Academic Press, 2nd Edition, (2003).

[17]. S. Cavalieri *et al.*, *Phys. Rev. A*, **55**, 2941, (1997).

[18]. M. Protopapas, C. H. Keitel, and P. L. Knight, *Rep. Prog. Phys.*, **60**, 389, (1997).

Chapter 5:

[1]. E. Hertz *et al.*, *Phys. Rev. A*, 64, 051801, (2001).

[2]. E. Goulielmakis *et al.*, *Appl. Phys. B*, **74,** 197, (2002).

[3]. N. A. Papadogiannis *et al.*, *Optics Lett.*, **27**, 1561, (2002).

[4]. C. R. Munnerlyn, *Appl. Opt.*, **8**, 827, (1969).

[5]. J.-C. M. Diels and W. Rudolf, *Ultrashort Laser Pulse Phenomena*, (Academic Press, 1996).

[6]. S. F. Fulghum and M. M. Tilleman, *J. Opt. Soc. Am.* B, **8**, 2401, (1991).

[7]. X. F. Li *et al.*, *Phys. Rev. A*, **39**, 5751, (1989).

[8]. C. Altucci *et al.*, *J. Opt. Soc. Am. B*, **13**, 148, (1996).

Appendix A:

[1]. R. Loudon, *The Quantum theory of Light*, 2nd Edition - Oxford Science, Oxford, (1991).

[2]. R. W. Boyd, *Nonlinear Optics,* (Academic press, Second Edition, 2003).